Investigating atmospheric scintillation using NGTS photometry of bright stars

by

Sean Mark O'Brien

Thesis

Submitted to the University of Warwick

for the degree of

Master of Science By Research

Department of Physics

September 2021

Contents

List of Tables

List of Figures

Acknowledgments

I feel incredibly lucky to have had the opportunity to undertake this unusual, semi-virtual Master's and wish to thank those who made this thesis possible.

I would first like to thank my supervisor, Dr. Daniel Bayliss, for being so enthusiastic from our first meeting to our most recent. I will be forever grateful to you for agreeing to take on this Maths undergrad with a re-discovered passion for astronomy. Thank you for guiding me through the project; helping me to secure a PhD position and also for all the cycling chat!

Thank you to everyone from Warwick Astro (and beyond) for accepting me into the group and making this year feel somewhat less odd. Thanks for all the tips and tricks you've given me and for putting up with my constant sports chat (sportsball is leaking). I hope one day I will meet you all in person!

I must extend special thanks to Ed for putting up with my endless questions; Ares for forging the MSc path and speaking so positively about the course and group; and Faith for being the best (and admittedly only) office mate I had. I wish I could thank many more amazing people here.

Thanks to all my friends and family who have shown (or politely feigned) interest in my astronomy endeavour, I'll be in Belfast for 4 years so don't all rush over at once (but please do come visit!)

Finally, thank you to my parents for never discouraging me from pursuing my interests and for allowing me to move back home and take over the office. And to my brother Michael, for making me laugh all these years and keeping me distracted from 'The Science' when needed.

Declarations

I declare that the work presented in this thesis is my own except where stated, and has not been submitted to any other academic institution for any other degree or qualification. The research was undertaken at the University of Warwick, during the period October 2020 to September 2021, under the supervision of Dr. Daniel Bayliss.

The work in this thesis has been submitted for publication in the Monthly Notices of the Royal Astronomical Society (MNRAS) on 2021 August 17 under the title: 'Investigating atmospheric scintillation using NGTS photometry of bright stars.' In particular:

- **Chapter 1:** Section 1.2 is based on Sections 1 and 2 of O'Brien et al. (2022);

- **Chapter 2:** Based on Section 3 of O'Brien et al. (2022);

- **Chapter 3:** Copied with minor edits from Section 4.1 of O'Brien et al. (2022);

- **Chapter 4:** Copied with minor edits from Section 4.2-4.5 of O'Brien et al. (2022);

- **Chapter 5:** Based on Section 5 of O'Brien et al. (2022) with the addition of Section 5.1.

I wish to thank all co-authors of the above work for their useful feedback and suggestions during the project. In particular, thank you to Peter Wheatley and James Osborn for their invaluable expert comments during the project.

Data Acknowledgments

Abstract

Atmospheric scintillation is expected to dominate photometric noise for ground-based high-precision photometry of bright stars using small telescopes. I use 122 nights of Next Generation Transit Survey (NGTS) photometry of bright stars ($G_{\mathrm{mag}} \lesssim 11.5$) to study the effect of scintillation and compare it with theoretical noise models. I verify that scintillation is indeed the dominant source of photometric noise for these stars. I determine a median scintillation coefficient at the Paranal Observatory of $C_{\mathrm{Y}} = 1.54$, which is in good agreement with previous results derived from MASS-DIMM measurements at the VLT. I find that separate NGTS telescopes make consistent measurements of scintillation when simultaneously monitoring the same field. Using contemporaneous meteorological data, I find that higher wind speeds at the tropopause correlate with a decrease in long-exposure ($t = 10\,\mathrm{s}$) scintillation. Hence the winter months between June and August provide the best conditions for high precision photometry of bright stars using small telescopes at the Paranal Observatory. This work demonstrates an alternative to the MASS-DIMM method for measuring the scintillation conditions at astronomical observatories by using bright star photometry.

Abbreviations

ADU	Analog to Digital Unit
ASM	Astronomical Site Monitor
CCD	Charge-coupled device
ECMWF	European Centre for Medium-Range Weather Forecasts
ESO	European Southern Observatory
FITS	Flexible Image Transport System
MASS-DIMM	Multi-Aperture Scintillation Sensor-Differential Image Motion Monitor
NGTS	Next Generation Transit Survey
SCIDAR	SCIntillation Detection And Ranging
RMS	Root mean square
TESS	Transiting Exoplanet Survey Satellite
VLT	Very Large Telescope
WASP	Wide Angle Search for Planets

Chapter 1

Introduction

> 'When I meet God, I am going to ask him two
> questions: Why relativity? And why turbulence? I
> really believe he will have an answer for the first.'
>
> —Werner Heisenberg (allegedly) (Marshak and
> Davis, 2006)

One of the first things we notice when staring at the night sky is that all the stars flicker. This behaviour is described to younger audiences with the lullaby 'Twinkle, twinkle, little star' and is arguably captured in van Gogh's 'The Starry Night' (see Figure 1.1), which may be more scientific than it first appears (Beattie and Kriel, 2019).

Many explanations of the twinkling of stars have been postulated in the past. Most notably, Aristotle proposed the following explanation for why stars (fixed stars) twinkle, while planets (wandering stars) do not:

> 'The planets are near us, so that the visual ray (a supposed ray that extends
> from the eye to an object) reaches them in its full vigour, but when it comes
> to the stars it is quivering because of the distance and its excessive extension,'

taken from Ellison (1952)'s translation of Aristotle's *De Caelo* (Aristotle, 350 BC). We shall see that Aristotle's explanation is not so far from the truth as the proximity of the planets is the reason they do not noticeably twinkle.

The technical term for this 'twinkling' is *atmospheric scintillation* and it is caused by turbulence in the Earth's atmosphere. The turbulence disrupts the path of starlight and changes the intensity of light (flux) we see or measure by deflecting the light into and out of our eye's pupil or telescope aperture, see Section 1.2 of this thesis and Dravins et al. (1997). These variations in the light intensity reduce the quality of the observations

Figure 1.1: Vincent van Gogh's The Starry Night, (van Gogh, 1889). van Gogh's oil-on-canvas painting of the view from his asylum window in Saint-Rémy-de-Provence. Could these swirls depict turbulence?

we are able to make with telescopes, therefore it is often referred to as *scintillation noise* and it is desirable to try and mitigate the effects of it (Osborn et al., 2011; Viotto et al., 2012; Osborn, 2015). In order to do so we must gain a better understanding of the level of scintillation at astronomical observatories and what factors, both atmospheric and technical, effect it.

The twinkling of stars also provides amateur astronomers with a quick way to spot the other planets in our Solar System. The planets are near enough to Earth that they are resolvable as small disks on the sky, whereas stars are so distant that they are referred to as 'point-sources.' The light from the planets is still distorted by Earth's atmosphere but the distortions cancel each other out across the disk so the planets do not appear to flicker on the night sky. Indeed the brightest 'star' to the right of cypress tree in 'The Starry Night' (Figure 1.1) is actually Venus (Whitney, 1986). While we have known of the existence of other planets in our solar system since the 2nd millennium BC (Sachs, 1974), the idea of planets outside our solar system only originated in the 16th Century when Italian philosopher Giordano Bruno speculated: 'This space we declare to be infinite... In it are an infinity of worlds of the same kind as our own,' (Bruno, 1584).

The first exoplanet was only discovered in 1992, some 400 years later, around a rapidly rotating neutron star (Wolszczan and Frail, 1992). This was quickly followed by the first exoplanet around a Sun-like star in 1995 with 51 Pegasi b (Mayor and Queloz, 1995). However, while over 4000 exoplanets have been discovered since then[a], it is believed that there could be at least one planet per star in the Milky Way (Cassan et al., 2012) which would mean a minimum of 10^{11} planets in our Galaxy alone. We are only scratching the surface of exoplanet discoveries and in order to find more, we must improve our detection capabilities.

Bright stars are relatively simple to observe compared to fainter objects, however observations of bright stars are dominated by scintillation when observing from the ground (Föhring et al., 2019). One solution is to bypass the atmosphere completely by placing our telescopes in space, e.g. Kepler (Borucki et al., 2010) and the Transiting Exoplanet Survey Satellite (TESS; Ricker et al. (2015)), but this is much more expensive than building ground-based telescope facilities. Thus, if we are to detect more exoplanets using ground-based telescopes, such as the Next-Generation Transit Survey (NGTS; Wheatley et al. (2018); Section 2.1), then we must work to understand scintillation as it is reducing our ability to detect exoplanets.

The following two paragraphs are derived from the Introduction (Section 1) of O'Brien et al. (2022).

---

[a]See the NASA Exoplanet Archive: `https://exoplanetarchive.ipac.caltech.edu/`

In addition to improving exoplanet detection capabilities, the study of scintillation is also of interest to those working in the field of asteroseismology where flux variations are of the order 0.01 to 0.1% (Brown and Gilliland, 1994; Heasley et al., 1996). Additionally, characterisation of the optical turbulence above astronomical sites is also of interest for those developing scintillation correction techniques (Osborn et al., 2011; Viotto et al., 2012; Osborn, 2015; Dhillon et al., 2016). Furthermore, satellite communications that involve the use of lasers passing through the atmosphere, in order to transmit data to the ground, depend on an accurate model for optical turbulence and scintillation (Andrews and Phillips, 2002; Jiang et al., 2020).

In this thesis, I measure atmospheric scintillation above ESO's Paranal Observatory by analysing NGTS photometric[b] data for a sample of around 22,000 observations of bright stars. Observations consist of the monitoring of a bright star in the field-of-view of an NGTS telescope for more than 2.4 hours on a given night. To define bright stars I use Gaia magnitudes (G_{mag}; Gaia Collaboration et al., 2016), selecting stars with $G_{\mathrm{mag}} \lesssim 11.5$. This threshold magnitude was selected to match where the photometric noise is dominated by the scintillation effect for NGTS photometry (Wheatley et al., 2018).

1.1 Exoplanet Transit Detection

This section briefly describes the exoplanet transit detection method, which is the primary astronomical observing technique that will benefit from the results of this project.

The most prolific method for detecting exoplanets to date has been the transit method with 3432 out of the 4514 exoplanets discovered so far being from transit surveys[c]. The transit detection method is simple in principle. The amount of light emitted by a star can be measured by telescopes using photometry. When a planet orbiting the star passes in front of the star, this causes a dip in the intensity of light we measure for the duration of the transit, see Figure 1.2.

The depth of a transit (i.e. the amount the brightness dips due to the planet) provides us with a way to measure the radius of a planet using the following equation from Winn (2010),

$$\frac{\Delta f}{f} \approx \frac{\pi R_p^2}{\pi R_*^2} = \left(\frac{R_p}{R_*}\right)^2. \tag{1.1}$$

---

[b]**Photometry**: measurement of flux or light intensity of astronomical objects. From the Greek *photo* meaning light and *metry* meaning measure

[c]Correct as of September 2021
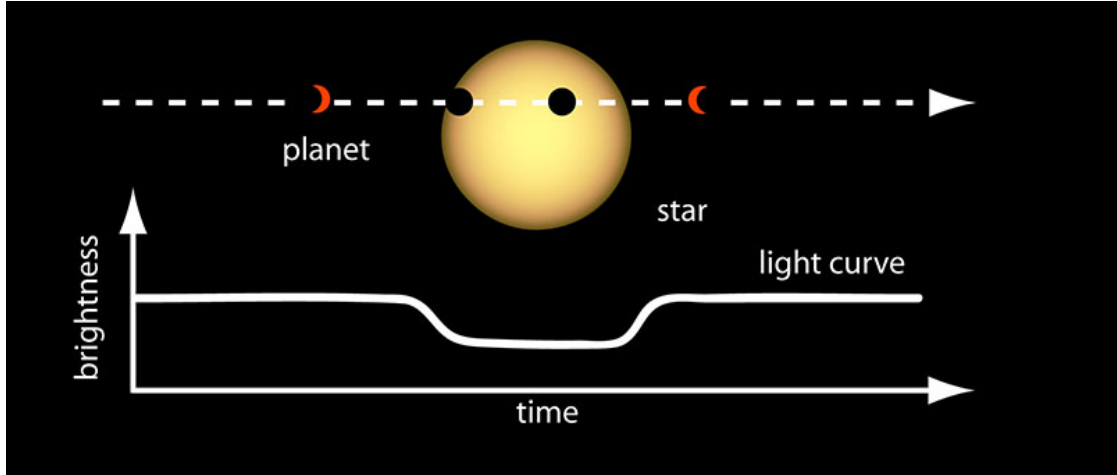
Figure 1.2: Diagram of a planet transiting its star and the light curve that would be measured. *Credit: NASA Ames*

The fractional change in brightness, f, is approximately the ratio of the area of the disk of the planet to that of the star, which equals the square of the ratio of their radii. Stellar radii can be determined from other observations such as comparing the stellar spectrum to models to determine effective temperature of the star, which when coupled with distance to the star and brightness allows us to use standard modelling equations to determine R_*. Brightness, or flux, is typically normalised to a value of 1 and Δf is determined from the light curve of the transit, as shown in Figure 1.2.

Observing multiple transits allows us to measure the orbital period of a planet. Additional follow-up observations can determine planetary mass using the radial velocity technique, which measures the gravitational wobble induced on a star by the orbiting planet. Mass and radius measurements allow us to calculate the bulk density which informs us of whether the planet is likely to be rocky (like Earth) or gaseous (like Jupiter). A non-exhaustive list of other exoplanet detection methods include: transit-timing variations (Bryant et al., 2021), direct imaging (Marois et al., 2008) and astrometry (Perryman et al., 2014).

1.2 Scintillation

The remainder of this chapter is dedicated to explaining the causes and effects of atmospheric scintillation.

Kolmogorov turbulence theory

The Earth's atmosphere is a dynamic environment that changes rapidly and is difficult to predict (see Section 2.3). The most chaotic feature of the atmosphere is turbulence and it is this turbulence which causes scintillation, disrupting the light from a star in the same way an aeroplane is buffeted about. The turbulent flow of a fluid is not fully understood and remains one of the great unsolved problems of physics. The equations which govern smooth fluid flow are believed to describe turbulent flow also, however this has not been mathematically proven (Lerner and Trigg, 1991). Numerical solutions to these equations for turbulent flow are computationally very expensive so we must rely on simpler models. The most complete model for turbulence is *Kolmogorov's theory of 1941* (Kolmogorov, 1941) which assumes energy is injected into a turbulent medium on large spatial scales, L_0, and forms eddies. Eddies are the swirling features of a fluid which then break down into smaller eddies in an energy cascade until they reach a spatial scale, l_0, when the energy is dissipated due to friction. In the case of atmospheric turbulence, the energy is injected by solar heating and wind shear at the top of the troposphere, known as the tropopause, which is around 10-12 kilometre above the Earth's surface (Roddier, 1981; Osborn, 2010).

Jet streams

Wind shears at the tropopause occur frequently due to the jet streams. Both the northern and southern hemisphere have two distinct jet streams each, the polar jet streams and the subtropical jet streams. These are high speed air currents in the upper atmosphere which flow west to east (westerly), often in a disjointed manner at speeds up to $123 \mathrm{~m\,s^{-1}}$ but more typically around 30-50 $\mathrm{m\,s^{-1}}$ (Archer and Caldeira, 2008). Figure 1.3 shows a cross section of the standard global circulation model with the Hadley Cell, Ferrel Cell and Polar cell which redistribute air in the atmosphere across different latitudes. The jet streams sit in the boundaries between the cells, as indicated in the diagram. The same model is mirrored in the southern hemisphere.

The southern hemisphere subtropical jet stream is most important to this work as it is typically found around a latitude of 30°S although this varies throughout the year, as shown in Section 2.3. The Paranal Observatory in Chile, where the NGTS telescopes are located (Section 2.1), is at a latitude of 24.6°S so observations are often made while the subtropical jet stream is overhead (Archer and Caldeira, 2008). This is the source of the wind shearing that causes the turbulence high above Paranal which

---

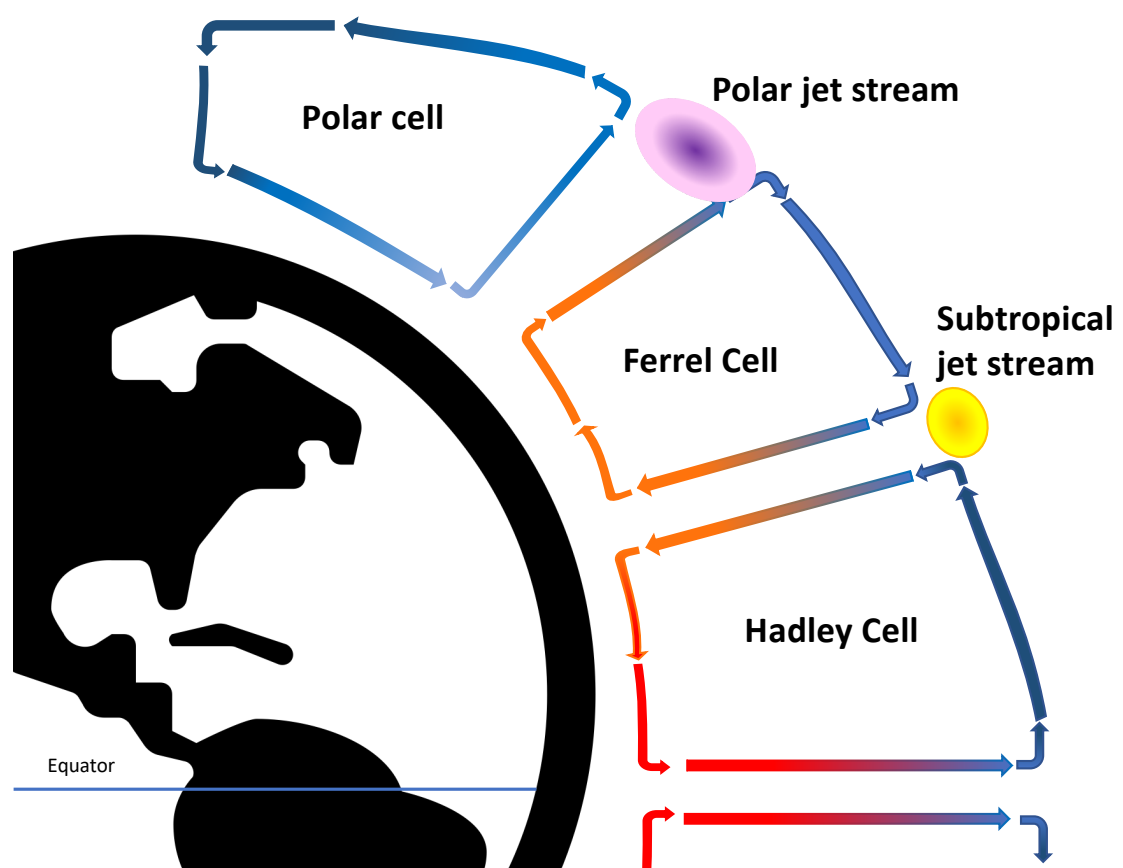[d] https://www.weather.gov/jetstream/jet

Figure 1.3: Cross section showing the northern hemisphere jet streams above the Americas with the three-cell circulations displayed also. Credit: Own work based on NWS image[d].

then causes the scintillation that affects our observations. The role of the jet stream and other high altitude winds is also important when we look at how the exposure time of our observations affects the level of scintillation we measure, see Section 1.2.1 and Section 4.4.

Scintillation effect

When we observe from the ground, light from stars is distorted as it passes through turbulent regions of the Earth's atmosphere. Differences in air temperature in the atmosphere, due to circulation and Solar heating, cause differences in the density and therefore refractive indices of these regions. This in turn causes phase distortion of a plane light wave passing through the turbulent layers. As the light propagates through the atmosphere, the phase distortion increases and the wavefront interferes with itself resulting in both phase and intensity fluctuations. The spatial distortion of the point-spread function due to phase aberrations is the familiar concept of 'seeing' which can be corrected through the use of adaptive optics (Babcock, 1953). However, when observing bright stars using small-aperture telescopes the dominant noise source can be atmospheric scintillation. Scintillation is the resulting variations in intensity of the light received by a telescope, due to the effects of the atmosphere (e.g. Dravins et al., 1997). These variations are typically of the order 0.1–1.0% (Osborn et al., 2015; Föhring et al., 2019) which is similar to the depth of exoplanet transits or asteroseismology signals. Figure 1.4 which is taken from Osborn et al. (2011) shows a schematic diagram of the scintillation effect and includes the speckling that is seen on the pupil image due to scintillation.

The magnitude of the intensity speckles is directly linked to the propagation distance of the distorted wavefront from the turbulent layer. The further the light propagates, the more it can interfere with itself (Osborn, 2010). Therefore, higher altitude turbulence is usually the primary cause of scintillation and it is not dominated simply by the strongest turbulent layer of the atmosphere that is typically the layer nearest the ground (Osborn et al., 2015). Equations (1.3) and (1.4) in Section 1.2.1 make this more apparent. This phenomenon is contrary to the reasoning for the more commonly discussed topic of astronomical seeing which is dominated by the strongest, ground-layer turbulence. This leads to confusion on the matter as both scintillation and seeing are caused by turbulence, but the difference in which layers are responsible means that it is possible to have poor seeing but good scintillation on the same night (Osborn et al., 2015).

8
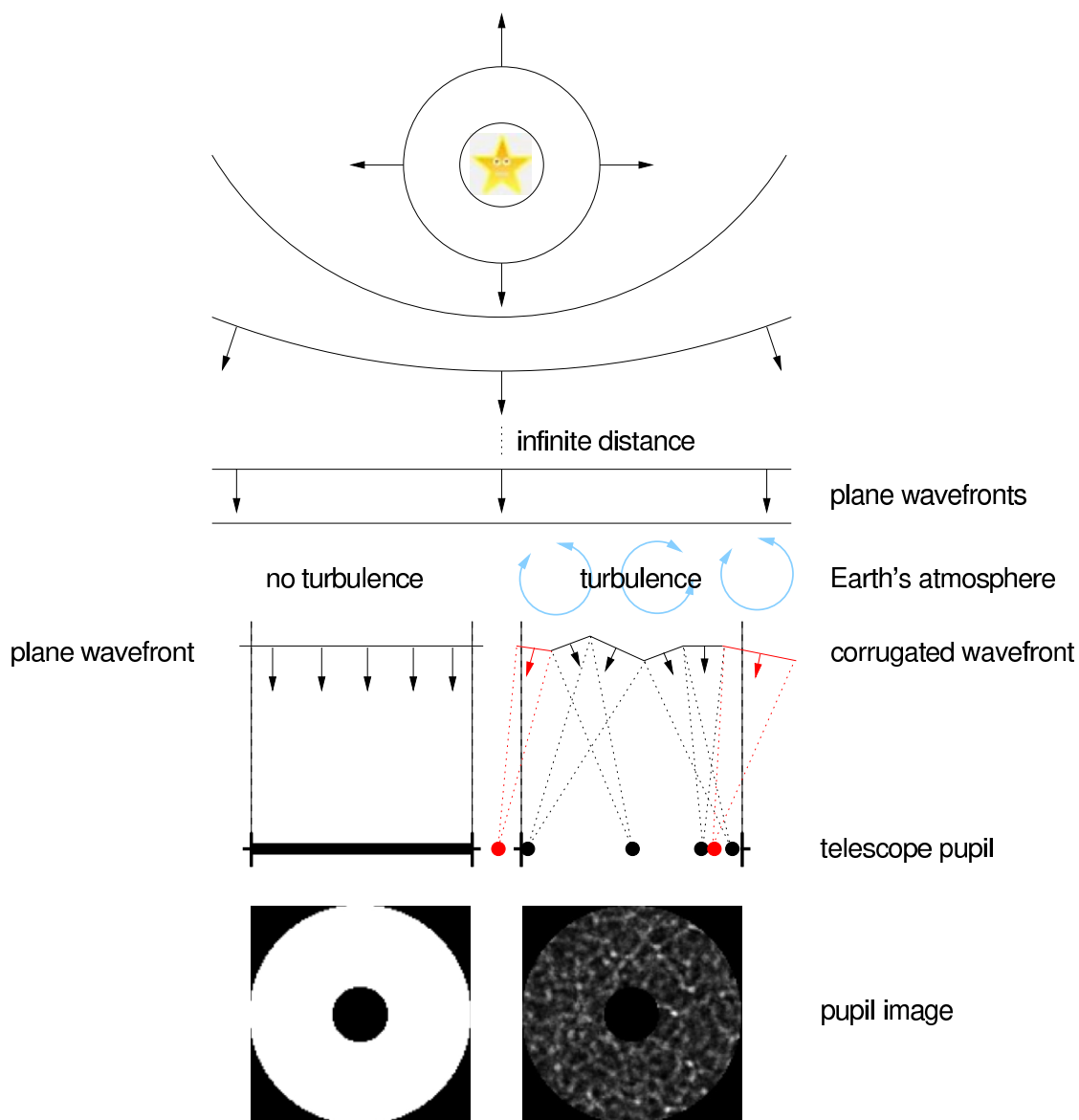
Figure 1.4: Schematic scintillation diagram. Light radiates from a star as a spherical wavefront. Once this reaches Earth it is essentially a plane wavefront entering the atmosphere. Without turbulence (left), the plane wavefront is collected by the telescope undisturbed. With turbulence (right), the wavefront is distorted as it passes through the atmosphere, creating a corrugated wavefront that interferes with itself resulting in intensity fluctuations. These intensity fluctuations are scintillation. This creates a speckled image on the telescope pupil. Figure from Osborn et al. (2011).

1.2.1 Effects on photometry

Methods for reducing the effect of scintillation on ground-based photometry, such as conjugate-plane photometry (Osborn et al., 2011), have been proposed in recent years, however the implementation of these methods is not widespread. An extreme solution to avoiding the scintillation effect entirely is to place our telescopes above the atmosphere, in space. NASA currently operates the TESS mission (Ricker et al., 2015) which surveys large sectors ($24° \times 96°$) for 27 days at a time in search of transiting exoplanets. Figure 1.5 shows a comparison between a transit event observed by TESS (space-based) and the same event observed by a single NGTS camera (ground-based, see Section 2.1). The exoplanet transit observed is WASP-166b, which orbits a star with an apparent magnitude of $G_{\mathrm{mag}} = 9.26$. This brightness is well within the regime where scintillation dominates the photometric noise model, see Section 3 for a description of other noise sources I consider. The authors of Bryant et al. (2020) demonstrate that higher quality observations are achievable when multiple NGTS telescopes are used to observe the same transit event.

It is immediately evident from Figure 1.5 that the photometric noise is much higher when observing from the ground. Automated algorithms would likely be unable to detect the transit observed from the ground without an extended period of observations that could cover more transits. The primary issue with space-based observatories is the financial cost. TESS is regarded as relatively cheap at \$200 million (Ricker et al., 2015), however NGTS cost a fraction of this and it is much more straightforward to repair and service a ground-based facility. Figure 1.5 highlights the importance of understanding and mitigating the effects of scintillation.

The modified Young's equation

The fractional amplitude of photometric noise due to scintillation (σ_{Y}) can be estimated using the modified Young's approximation (Young, 1967; Osborn et al., 2015),

$$\sigma_{\mathrm{Y}}^2 = 10 \times 10^{-6} C_{\mathrm{Y}}^2 D^{-4/3} t^{-1} (\sec z)^3 \exp\left(-2h_{\mathrm{obs}}/H\right), \qquad (1.2)$$

where D is the diameter of the telescope aperture (m), t is exposure time used (s), h_{obs} is the altitude of the observatory (2440 m for Paranal), H is the scale height of the atmospheric turbulence, taken to be 8000 m. z is the zenith distance, and therefore $\sec z$ approximates airmass. C_{Y} ($\mathrm{m}^{2/3}\mathrm{s}^{1/2}$) is the empirical coefficient.

This equation is taken from Osborn et al. (2015), where they introduced the
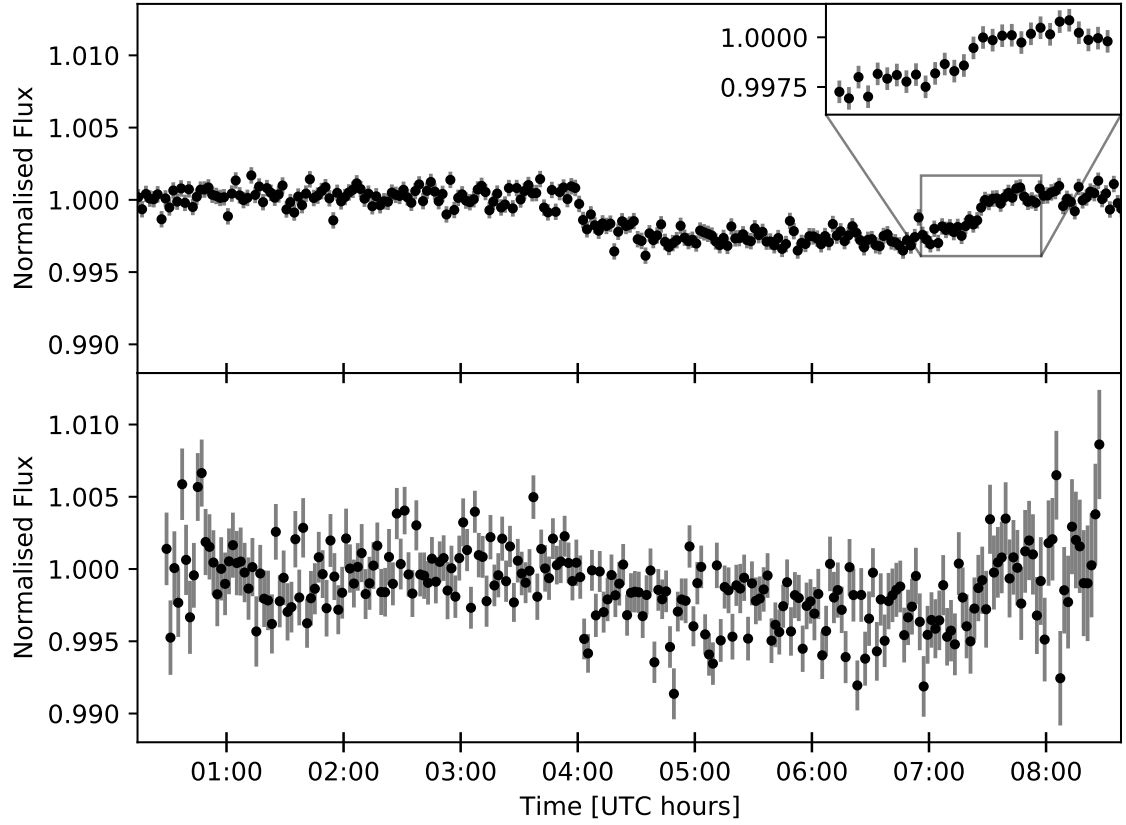
Figure 1.5: *Top panel*: TESS light curve for WASP-166 on 2019 February 25 showing the transit of WASP-166b from UTC 04:00 until UTC 7:30. *Inset*: Zoomed section of the egress of the transit showing the relative size of the TESS error bars. *Bottom panel*: NGTS light curve for a single camera for WASP-166 on 2019 February 25.

empirical coefficient, C_Y, to improve the original empirical model from Young (1967). This C_Y is typically found to be around 1.5 for different sites, however this is a median value and the actual value can vary significantly across even a single night of observing (Osborn et al., 2015). The median measured value of C_Y at the Paranal Observatory is $1.56^{+0.34}_{-0.29}$, where the limits are the upper and lower quartiles. This value is taken from Osborn et al. (2015) where they extracted the results from data presented in Kornilov et al. (2012), where the authors originally identified that the Young's approximation underestimated scintillation by around 1.5 for most observing sites.

The long and the short-exposure scintillation indices

A more comprehensive measure of the scintillation index can be achieved using vertical profiles of the refractive index structure constant of the atmosphere, $C_n^2(h)$, and the wind velocity. The exposure time of the observations can cause differences in the level of scintillation measured and therefore we use different equations to model this. For short-exposure observations, there is no temporal averaging of the intensity speckles that cause scintillation. In the long-exposure regime, the intensity speckles traverse the telescope pupil and scintillation reduces due to temporal averaging, with a dependency on high-altitude wind speed (Osborn et al., 2015). The crossover between the short-exposure and long-exposure regimes is determined to be approximately 0.01-0.1 s by Osborn et al. (2015), although this will depend on telescope diameter, airmass, wind direction and the wind velocity profile. This is evident from Equations 1.3 and 1.4 which follow. NGTS (Section 2.1) uses 10 second exposures and so operates in the long-exposure regime, thus if turbulence profilers were active at Paranal consistently then I could use the following equation given by Kenyon et al. (2006); Osborn et al. (2015),

$$\sigma_{I,\mathrm{le}}^2 = 10.66 D^{-4/3} t^{-1} (\sec z)^\alpha \int_0^\infty \frac{h^2 C_n^2(h)}{V_\perp(h)} \mathrm{d}h, \qquad (1.3)$$

where $C_n^2(h)$ is the profile of the refractive index structure constant, h is the altitude of the turbulent layer, $V_\perp(h)$ is the wind velocity profile and α is the exponent of the airmass which varies between 3 for wind transverse to the azimuthal angle of the star, and 4 for longitudinal wind. The h^2 term in the integral of this equation demonstrates that turbulence at higher altitudes has a greater effect on the scintillation measured by a telescope, as described in Section 1.2.

The Multi-Aperture Scintillation Sensor (MASS)-Differential Image Motion Monitor (DIMM) instruments (Section 2.2) use a short exposure of around 1 ms to measure the intensity variation and derive scintillation indices. This is in the short-exposure scin-

tillation regime. If provided with a turbulence profile, the short-exposure scintillation index is calculated as,

$$\sigma_{I,\mathrm{se}}^2 = 17.34 D^{-7/3} (\sec z)^3 \int_0^\infty h^2 C_n^2(h) \mathrm{d}h. \qquad (1.4)$$

MASS-DIMM data are available every night although I do not directly implement the above equation as the ESO data portal provides scintillation indices directly. It has been demonstrated that at sites such as Paranal, the long-exposure scintillation index, $\sigma_{I,\mathrm{le}}$, is minimal between May and September, meanwhile the short-exposure scintillation index, $\sigma_{I,\mathrm{se}}$, is maximal during this period (Kornilov et al., 2012). In this thesis, I investigate whether there exists a similar seasonal dependence in the scintillation measurements made with NGTS.

Chapter 2

Data

> I've never owned a telescope, but it's something I'm thinking of looking into.

In this chapter, I describe the three main sources of data that were used in the subsequent analysis of this project. The Next Generation Transit Survey (NGTS; Section 2.1); the Paranal Astronomical Site Monitor (ASM; Section 2.2); and the European Centre for Medium-Range Weather Forecasts (ECMWF; Section 2.3).

2.1 Next Generation Transit Survey

The Next Generation Transit Survey (NGTS; Wheatley et al. (2018)) is an array of twelve telescopes with $20\,\mathrm{cm}$ diameters, primarily designed to search for transiting exoplanets (Section 1.1) orbiting bright stars by using the photometry technique. The telescope facility (see Figure 2.1) is installed at the European Southern Observatory (ESO) at Cerro Paranal, Chile and is located around $2\,\mathrm{km}$ from the Very Large Telescope (VLT). The latitude and longitude of the observatory is $(\phi, \lambda) = (24.6°\mathrm{S}, 70.4°\mathrm{W})$ which means it is typically at the same latitude as the southern hemisphere subtropical jet stream described in Section 1.2. The telescopes are operated by a consortium of UK and European institutes, including the University of Warwick, as well as members of the Chilean astronomical community and external collaborators. The project has built on the knowledge gained from the Wide Angle Search for Planets (WASP) Project (Pollacco et al., 2006), which is the most successful ground-based transit survey to date, discovering 148 of the 375 exoplanets that have been discovered by ground-based transit detectors.

Figure 2.1: The 12 NGTS telescopes on their mounts in the enclosure at ESO Paranal. *Credit: ESO/R. West*

Each NGTS telescope has a field of view of $8\,\mathrm{deg}^2$ which gives the full array a combined field of view of $96\,\mathrm{deg}^2$, for reference the Moon has an angular diameter of around $0.5\,\mathrm{deg}$. The primary goal of NGTS was to survey large sections of the sky in search of exoplanet transits (e.g. Bayliss et al., 2018). Since 2018, NGTS has also been used for exoplanet follow-up observations of bright stars, particularly from the TESS mission (Ricker et al., 2015). The very wide field of view of the NGTS telescopes gives them a unique capability amongst ground-based telescopes of being able to reach $150\,\mathrm{ppm}$ per 30 minutes for very bright stars (Bryant et al., 2020). The wide field of view allows NGTS to observe more stars of similar magnitude to the target stars. Stars of similar magnitude are better for use as comparison stars for relative photometry (see Section 2.1.1 and Chapter 3). The use of multiple telescopes simultaneously improves the precision further, see Figure 2.2. This has resulted in NGTS being used in the follow-up of bright stars, for example in refining the parameters for bright candidates from TESS (Armstrong et al., 2020; Brahm et al., 2020) and monitoring transit timing variations for bright stars (Bryant et al., 2021).

A custom photometric filter with a bandpass from 520 to $890\,\mathrm{nm}$ is used as it is optimal for observing the late K and early M dwarfs that NGTS targets. The telescopes are fitted with 2048×2048 pixel charge-coupled devices (CCDs) which have a read noise of around 14 electrons and a readout time of $3\,\mathrm{s}$, which coupled with the nominal $10\,\mathrm{s}$ exposure time of the telescopes results in a cadence of $13\,\mathrm{s}$ (Wheatley et al., 2018).

The research project on which this thesis is based primarily utilises NGTS observations from November 2018 until February 2021 conducted as part of the Bright Stars Working Group which aims to follow-up exoplanet candidates around bright host stars. The results of this project will inform the NGTS operations team of how scintillation affects bright star observations; the typical conditions found at the observatory; the environmental factors which cause this scintillation and also the precision of the 12 telescopes.

2.1.1 Bright Stars observations and pipeline

NGTS has a range of operating modes and pipelines[a]. This project uses observations collected as part of the Bright Stars Working Group's efforts to follow-up bright stars that have candidate, or known, transiting exoplanets.

The intensity of light and position of where the light is coming from on the sky is measured by a device called a CCD. This device is commonly found in digital cameras

---

[a]**pipeline**: a series of computer programs that process raw data and output data products.
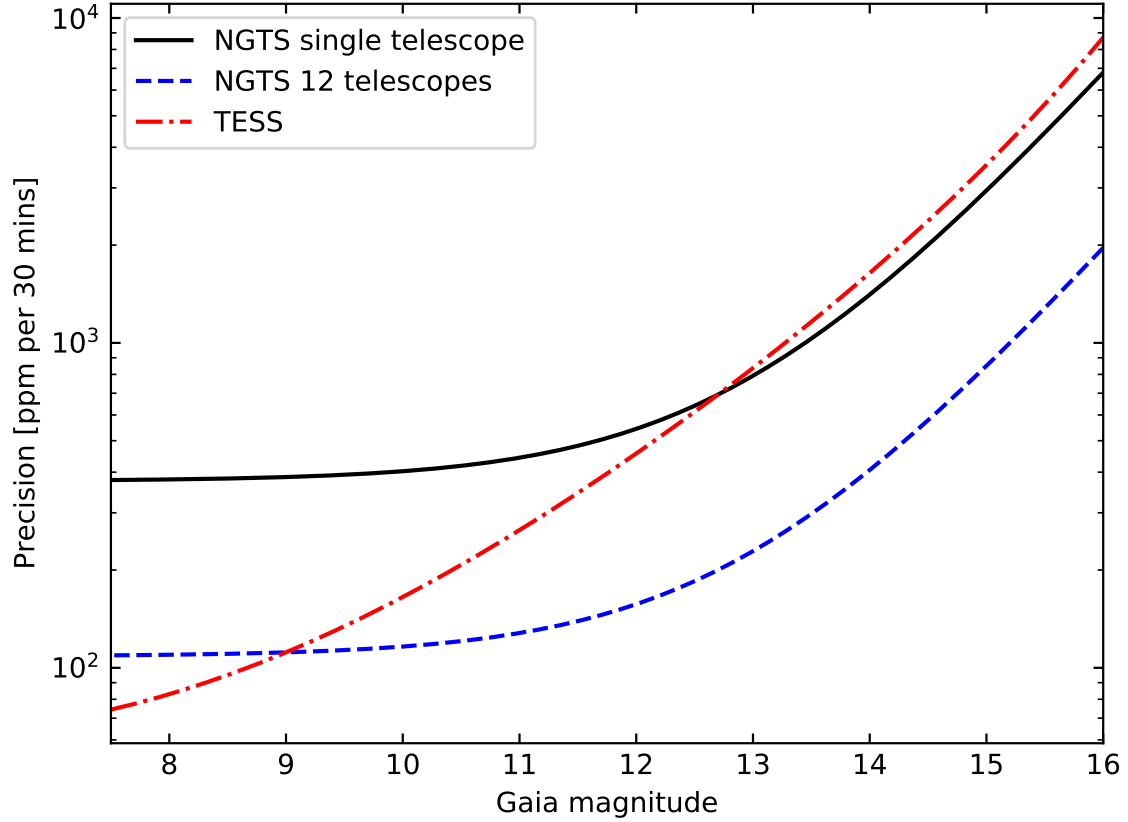
Figure 2.2: Comparison of the photometric precision of a single NGTS telescope; 12 NGTS telescopes; and TESS. Note the y-axis uses a logarithmic scale. A single NGTS telescope matches the precision of the space-based TESS instrument for dim stars ($G_{mag} > 12$). Atmospheric scintillation means that a single NGTS telescope is limited for bright stars, hence the higher values for the precision. Using 12 NGTS telescopes simultaneously greatly improves the precision of the observations, particularly at the bright end, and it is possible to reach 150 ppm per 30 minutes for bright stars.
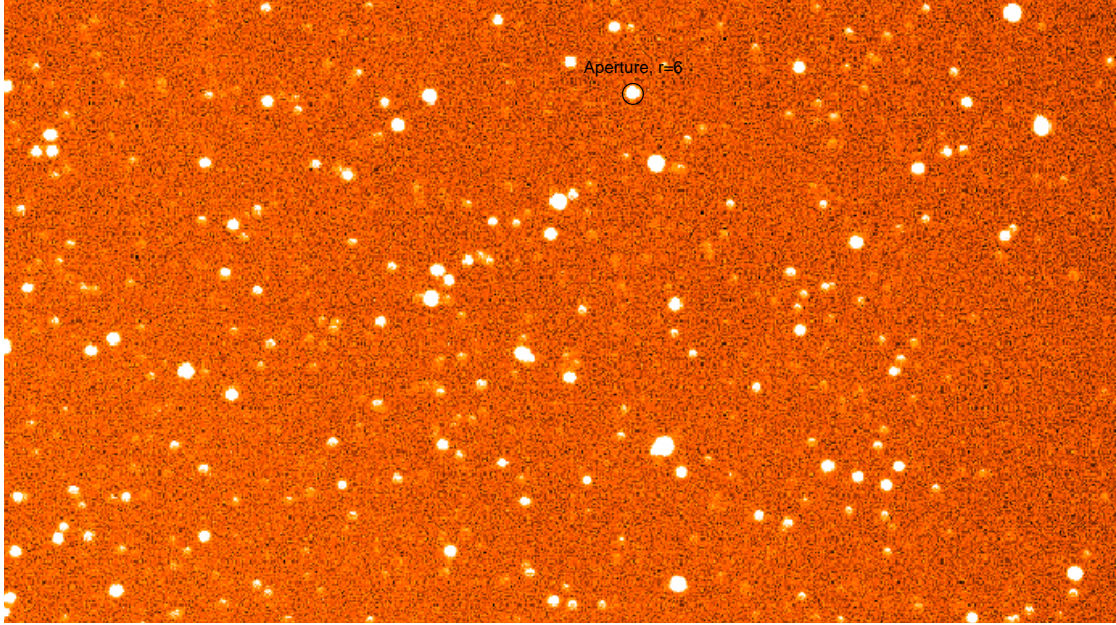
Figure 2.3: Section of a FITS image file generated by NGTS. The field of view is approximately $0.9° \times 0.5°$. This image was taken on 2019 November 14. Bright, white patches indicate a higher ADU count in these pixels, corresponding to the position of stars. A photometric aperture with radius of 6 pixels is superimposed on a star in the field.

and operates in a similar way in the NGTS telescopes. The basic description is that the CCD counts how many photons hit each pixel during the 10 s exposure time. The CCD measures this light intensity in Analog to Digital Unit (ADU) counts which do not match 1:1 with number of photons that reach the detector due to factors such as camera gain and quantum efficiency.

These exposures of the CCD are referred to as 'raw frames' and are processed by a custom NGTS pipeline that performs background subtraction where it is determined how many photons are due to sources other than the stars we are interested in. This generates a Flexible Image Transport System (FITS) file. These files essentially consist of a 2-dimensional array of numbers which correspond to the ADU counts on each pixel during the 10 s exposure time. Additional information on the operating conditions of the telescope and celestial coordinates of each pixel are also contained within the file. An example of a section of one of these FITS files is shown in Figure 2.3. This image was taken on 2019 November 14 during follow-up of a TESS Object of Interest, TOI-469. All bright star observations have a designated target star which is the star of interest in the field and likely will exhibit a transit event during the observation.

Due to the brightness of the stars we observe, the telescopes are often slightly defocused to avoid saturation of the CCD. Saturation occurs when too many photons hit a pixel such that the pixel cannot correctly count the light intensity upon it. During a single night of observation, one telescope can take approximately 2500 images which all undergo the same processing described.

Once the observations have been made and the FITS files are created, the pipeline carries out 'aperture photometry.' This step selects up to 100 comparison stars which are ranked by colour, brightness and position on the image relative to the target star. Circular apertures, such as the example shown in Figure 2.3, are placed on the image and the number of ADU counts due to the star, as well as the number of ADU counts due to the background, are measured. The pipeline performs this step for apertures with a range of radii, however I only use a radius of 6 pixels for my analysis because this is large enough to capture the full extent of the stars I observe. The end products of this pipeline are 'phot files' which contain information on timestamps and airmass along with positions, fluxes and various other parameters for each comparison star in the image, plus the target star. The files are typically 5-10 MB in size with 9 columns of standard data and 7 columns of parameters for each star. This gives approximately 200 to 700 columns of data per file, depending on the number of comparison stars. The files have approximately 2500 rows as each row corresponds to an image taken by the camera.

The bright star operation mode and pipeline are described by Bryant et al. (2020). Prior to the analysis steps that follow in Section 3, I remove the star targeted for observations due to the likelihood that it contains a transit event. This avoids the need for modelling and subtraction of the transit, without removing a significant number of stars from the sample.

2.2   Paranal Astronomical Site Monitor

The Paranal Astronomical Site Monitor (ASM; Chiozzi et al. (2016)) is a collection of instruments at the Paranal Observatory in Chile which monitor the current atmospheric conditions most pertinent to astronomical observations. In this work, I use data from the combined Multi-Aperture Scintillation Sensor (MASS)-Differential Image Motion Monitor (DIMM) instruments[b] (Kornilov et al., 2007). The MASS-DIMM sits next to UT4 (Yepun) of the VLT. The MASS-DIMM consists of two different instruments mounted to a single telescope, atop a tower shown in Figure 2.4.

---

[b]http://archive.eso.org/cms/eso-data/ambient-conditions/paranal-ambient-query-forms.html

Figure 2.4: The 7 m tall MASS-DIMM tower at Paranal Observatory. The Milky Way streaks across the top of the image while the zodiacal light (of rock and roll fame; May (2007)) illuminates the horizon and lines up with the tower in the foreground. *Credit: ESO/Y. Beletsky*

The MASS-DIMM instruments are used at most astronomical observing sites and were developed by Sternberg Institute, Russia and Cerro Tololo Observatory, Chile. Their construction and the theoretical background is described in detail in Kornilov et al. (2007), while the full ASM and specifics of the MASS-DIMM used at Paranal are described in Chiozzi et al. (2016). The MASS-DIMM at Paranal is mounted to a Celestron C11 telescope with a 28 cm diameter. The MASS is sensitive to high altitude turbulence while the DIMM measures the integrated turbulence. The difference between the two can be used to estimate the ground layer turbulence (Haguenauer et al., 2020).

The MASS uses a series of 4 concentric apertures with the central aperture being referred to as 'Aperture A.' The instrument uses photo-multiplier tubes, since surpassed by CCDs in most applications, to count photons over a 1 ms exposure time. This exposure time is within the short-exposure scintillation regime. The different apertures allow different scintillation indices to be derived from the intensity variation measured. These indices can then be combined with DIMM data and fitted with a model of turbulent layers at different altitudes to recover a optical turbulence profile (Kornilov et al., 2012). The scintillation index for the central circular aperture (aperture A) can be used for comparison to measurements of the scintillation made with NGTS. The MASS scintillation indices are detrended with respect to airmass. DIMM data contains information on the position of the target star of the MASS-DIMM instrument, thus we can use this to calculate the angle between the MASS-DIMM target and the center of the NGTS field. The MASS-DIMM target stars are very bright, $V \lesssim 2$, and are only observed below airmass 1.5, therefore the target star switches during the night and we must split the NGTS data accordingly (Kornilov et al., 2007). NGTS data products are numbered by an 'actionID,' corresponding to the telescope ID, field observed and night of observation. We split 'actions' into 'sub-actions' if the MASS-DIMM instrument changes target star during the night because this allows analysis of correlations between target proximity and scintillation measurements (Section 4.3).

The estimations of C_{Y} for the Paranal Observatory presented by Osborn et al. (2015) are derived from measurements made using the MASS by Kornilov et al. (2012). The measurements of $\sigma_{I,\mathrm{le}}$ at La Palma presented by Osborn et al. (2015) are estimated from real atmospheric profiles measured using the stereo-SCIntillation Detection And Ranging (SCIDAR) instrument described by Shepherd et al. (2014). I draw comparison to these measurements in Section 4.1. I do not directly use SCIDAR measurements and therefore do not described the instrument in detail here.

2.3 European Centre for Medium-Range Weather Forecasts

The European Centre for Medium-Range Weather Forecasts (ECMWF) is an intergovernmental organisation which operates as a research institute and a weather forecasting hub for Member States. The ECMWF maintains an archive of meteorological data that spans centuries and provides datasets on topics such as: glacial distributions; climate projections; and, pertinent to this work, atmospheric wind velocity.

In this work, I utilise the 'ERA5 monthly averaged data on pressure levels from 1979 to present' dataset (hereafter, 'ERA5 dataset'; Hersbach et al. (2019)). This data is a reanalysis of global weather that combines weather models with real observations from across the globe. This thesis uses information on the U (eastward) and V (northward) wind vector components at a constant pressure level of 250 hPa, which corresponds to where the subtropical jet stream lies, around 12000 meters above sea level (U.S. COESA, 1976; Archer and Caldeira, 2008). We can map the position of the jet stream above South America and also this allows us to calculate a monthly, quantitative measure of the mean wind speed above Paranal, which is important when considering the changes in both short-exposure and long-exposure scintillation indices (Kornilov et al., 2012; Osborn et al., 2015).

Figure 2.5 shows the typical pressure profile of the atmosphere and the altitudes where the polar and subtropical jet streams are found. The polar jet streams are typically at an altitude of 9000 to 12000 m whereas the subtropical jet streams are found in the range of 10000 to 16000 m (Archer and Caldeira, 2008). The equation for standard atmospheric pressure from U.S. COESA (1976) is,

$$p = p_0 \exp\left(-\frac{ghM}{T_0 R_0}\right), \tag{2.1}$$

where p is pressure in hectopascals and h is altitude in metres. $p_0 = 1013.25$ hPa is standard sea-level atmospheric pressure; $g = 9.80665 \,\mathrm{m\,s^{-2}}$ is the standard sea-level value of acceleration due to gravity; $M = 0.02896968 \,\mathrm{kg\,mol^{-1}}$ is the molar mass of dry air; $T_0 = 288.16$ K is the sea-level standard temperature of air; and $R_0 = 8.314462618 \,\mathrm{J\,mol^{-1}\,K^{-1}}$ is the Universal Gas Constant.

I elect to use the pressure level of 250 hPa to investigate the behaviour of the southern hemisphere subtropical jet stream. This choice was made from Figure 2.5 and because I tested pressure levels of 200 hPa and 225 hPa and found no significant difference in the subsequent analysis.
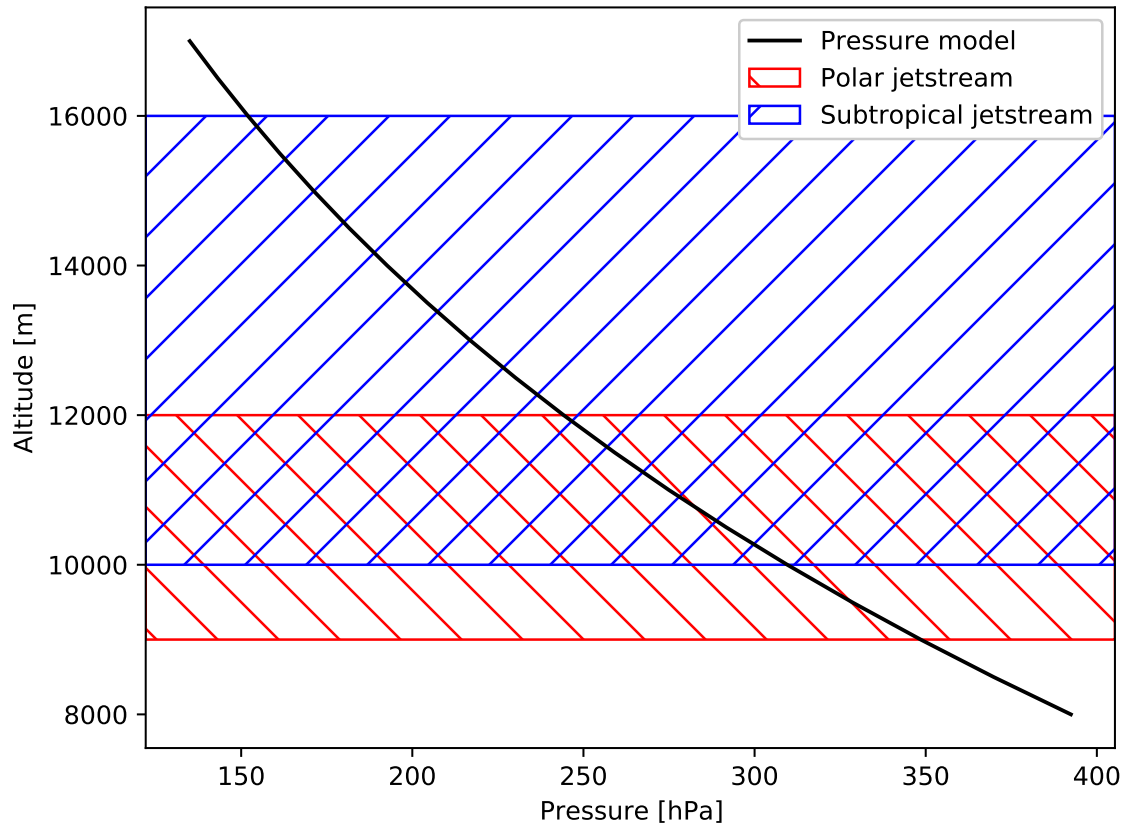
Figure 2.5: Plot of pressure in hectopascals against altitude in metres. The black solid curve indicates the standard pressure model, according to Equation 2.1. The hatched boxes indicate the typical altitudes of the polar (red) and subtropical (blue) jet streams.
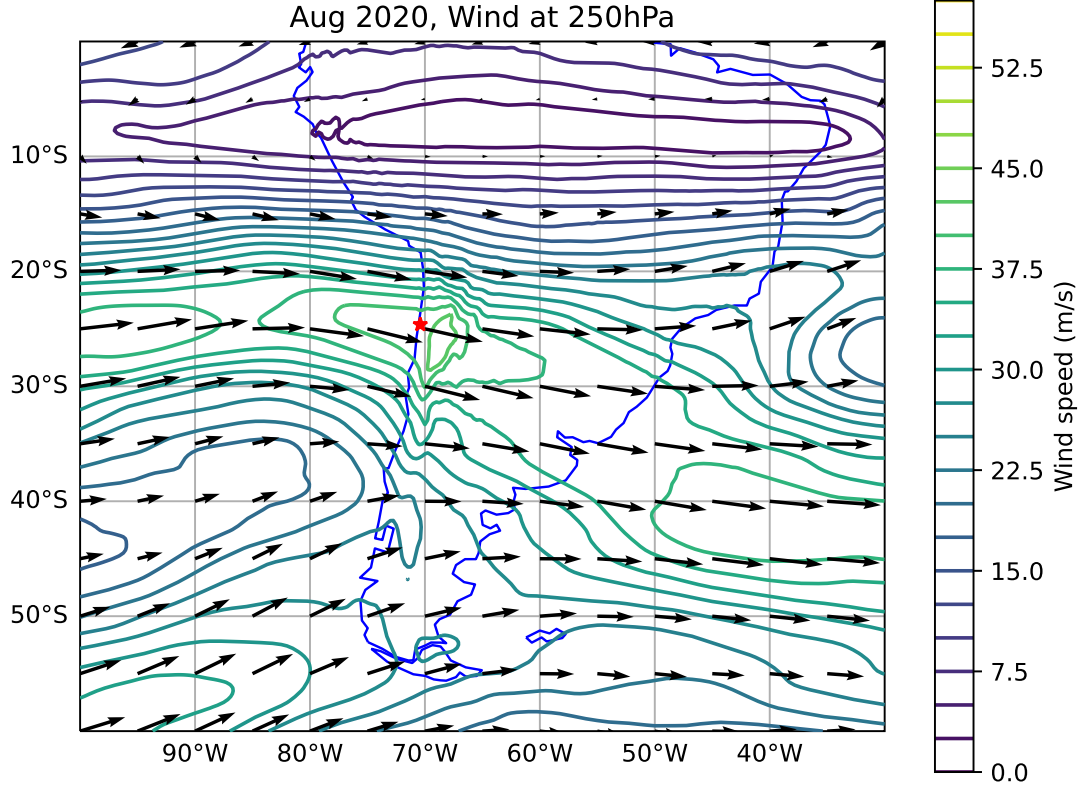
Figure 2.6: Wind velocity vectors (black arrows) and wind speed contours over South America (blue outline) for August 2020. The red star indicates the position of Paranal Observatory, the location of the NGTS telescopes $(\phi, \lambda) = (24.6°S, 70.4°W)$.

Figure 2.6 shows a snapshot of the data that can be extracted from the ERA5 dataset[c]. This figure shows the wind velocity vectors at 5 degree intervals, although the actual underlying data has a resolution of $0.25° \times 0.25°$. The wind velocity is presented as (U, V) vectors with positive U indicating eastward flowing wind and positive V indicating northward flowing wind. Wind speed at each point is calculated simply as $\sqrt{U^2 + V^2}$ and the resulting contours are plotted using a colourmap with contours at a resolution of $2.5\,\mathrm{m\,s^{-1}}$.

The subtropical jet stream is the dominant feature of the contours. It is the high speed channel of wind which starts at around 25°S, flows over Paranal Observatory (red star) and moves to more southernly latitudes of 40°S upon reaching 40°W. Disturbances in the high-altitude winds due to the Andes mountain range can be seen along the west

---

[c]Full animation: `https://astro-sobrien.github.io/mscthesis_gif.html`

coast of South America. These disturbances are the bumps in the contours perpendicular to the prevailing westerly wind direction. The Andes have an average height of $4000\,\mathrm{m}$ and peak at approximately $7000\,\mathrm{m}$. This is high enough that winds at the surface are driven upwards, but also outwards (i.e. northerly/southerly), by the mountains and this results in disturbances at higher altitudes (White et al., 2017). Part of the polar jet stream can be seen at 100°W to 80°W, above a latitude of 50°S, however this demonstrates the disjointed nature of the jet streams and also that the polar jet stream never reaches the latitude of Paranal.

It is important to recognise that Figure 2.6 is a **constant pressure map** showing wind direction and speed and that the wind direction is typically parallel to the contours. It is **not** a pressure chart which is more commonly used in weather forecasting, where wind direction is perpendicular to the pressure contour lines.

Chapter 3

Methods

Why did people not like the restaurant on the moon?

Because there was no atmosphere.

In this chapter I display light curves and a root mean square (RMS) curve (Figures 3.1a to 3.1c) taken from observations of a bright star (HD36109; $G_{\mathrm{mag}} = 8.04$) on 2020 January 28. These data were taken during NGTS follow-up observations of TOI-431 (Osborn et al., 2021).

Filtering

I process the raw NGTS light curves (Section 2.1) by first filtering out poor nights of observation (i.e. clouds passing across the line-of-sight) and stars with light curves that do not follow similar trends to other stars in the same photometry file, for example variable stars. This is achieved through a series of steps that fit polynomials to the raw light curves and compare coefficients of the models to check for any discrepancies. Stars that have model values differing greatly from the mean for the file are discarded. Next, stars with a measured mean flux below 30,000 ADU counts per exposure ($G_{\mathrm{mag}} \approx 11.5$) are removed as noise terms other than scintillation begin to dominate (Wheatley et al., 2018). Stars with mean flux values greater than 900,000 counts per exposure ($G_{\mathrm{mag}} \approx 7.5$) are removed due to the likelihood that they will saturate the NGTS CCD pixels. An example raw light curve is shown in Figure 3.1a.
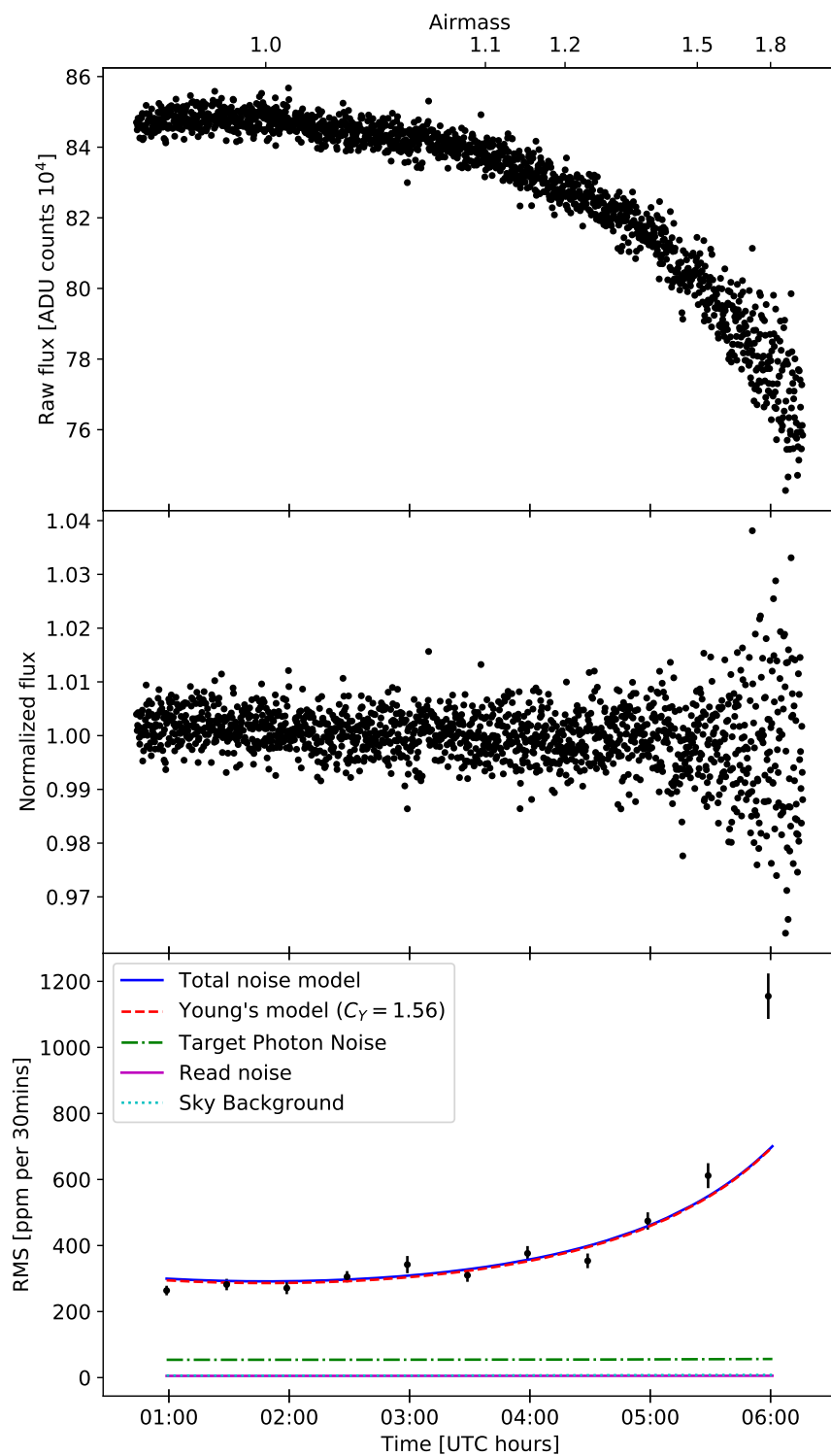
Figure 3.1: Caption on following page.

Top panel, Figure 3.1a: Raw NGTS light curve for a star observed on 2020 January 28. This star has a Gaia magnitude of $G_{\mathrm{mag}} = 8.04$ therefore the photometric noise is expected to be dominated by scintillation. Airmass is displayed on the top axis. Airmass started at around 1.03, decreased to 1.0 at approximately 2 am UTC, then increased to 1.98 at the end of the night. *Middle panel*, Figure 3.1b: Normalised light curve for the same star as above. Light curve is detrended and normalised via relative photometry. *Bottom panel*, Figure 3.1c: Photometric precision against time for the light curve shown above. The solid blue line is the total noise model (Eq. 3.3), the dashed red line which sits just below the total noise model is the modified Young's equation (Eq. 1.2) with the site median $C_{\mathrm{Y}} = 1.56$. The dark green dash-dot line is the target photon noise (Eq. 3.4), the dotted cyan line is the sky background (Eq. 3.5), the solid magenta line which almost coincides with the sky background is the read noise.

Normalisation

The light curves are normalised and then detrended using 'relative photometry.' This is achieved by constructing a master reference star which is the sum of the fluxes for all stars in the frame at each timestamp. I designate a 'current target star' which cycles through each star in the photometry file which has survived the filtering until all stars have a normalised flux calculated. I subtract the flux of the current target star, normalise both the target flux and the master flux by dividing each by their respective means. Finally I detrend the target flux by dividing normalised target flux by normalised master reference flux. This calculation is shown in Equation 3.1,

$$f_{*,norm} = \frac{f_*}{\bar{f_*}} \div \frac{f_m - f_*}{\overline{f_m - f_*}}, \tag{3.1}$$

where $f_{*,norm}$ is normalised flux of the current target star, f_* is the raw flux of the current target star, f_m is the master reference star flux and the mean values are indicated as $\bar{f}$.

Following the normalisation, stars with a particularly high RMS value across the full light curve, in comparison with the other stars in its frame, are removed as a final automated check for variable stars. An example normalised light curve is shown in Figure 3.1b.

The airmass trend is the dominant arching feature of the raw light curves, see Figure 3.1a. Higher airmass means we are looking through a larger column of air which leads to greater attenuation of light, as shown by the decrease in flux over the course of the night of observation. Furthermore, the greater spread of flux data points at higher airmasses, which is more apparent in the normalised light curve shown in Figure 3.1b, is due to stronger scintillation. This increase in scintillation is accounted for by the $(\sec z)^3$

term in Equation 1.2. The higher airmass, $\sec z$, means the distance to the turbulent layer is longer and so scintillation is increased as it is a propagation effect (Section 1.2).

RMS measurement

The next step is to calculate the RMS over 30 minute intervals across the normalised light curves. RMS, or standard deviation, is a measure of the amount of variation in a set of values. For a 30 minute interval of a normalised light curve, this is calculated as,

$$s = \sqrt{\frac{\sum_{i=1}^{N}(F_i - \bar{F})^2}{N}}, \tag{3.2}$$

where N is the number of flux values in the interval, F_i is the normalised flux at timestamp i and $\bar{F}$ is the mean normalised flux. I show a plot of these RMS values for the example light curve in Figure 3.1c. The values and error bars are calculated using bootstrap resampling (Astropy Collaboration et al., 2013, 2018). I take 10,000 samples with replacement of the normalised flux values for each 30 minute interval and compute the standard deviation on each of these samples, using Equation 3.2. The mean of the 10,000 standard deviations gives the RMS value for each 30 minute interval and the standard deviation of these standard deviations gives the error bars. Bootstrap resampling, or bootstrapping, is a common statistical method that allows the calculation of errors on RMS values.

Total noise model

Following McCormac et al. (2017), I calculate the total noise model as a combination of target photon noise, sky background, read noise and scintillation. Dark current, a small electric current in CCDs present even when no photons are incident on the device, is negligible as the NGTS cameras are sufficiently cooled to -70°C (Wheatley et al., 2018). The noise terms are computed in terms of ADU counts, therefore we must account for camera gain which ranges from 1.87 to 3.04 for the different NGTS cameras. The noise model used gives the total amount of noise, N_T, in ADU counts as,

$$N_T^2 = N_{\text{target}}^2 + N_{\text{sky}}^2 + (n_{\text{pix}} \times N_{\text{read}}^2) + (\sigma_{\text{Y}} \times f)^2. \tag{3.3}$$

The target photon noise is a statistical counting noise that is modeled by the Poisson process, it is calculated for the target star photons as,

$$N_{\text{target}} = \sqrt{\frac{f}{g}}, \tag{3.4}$$

where f is the source count rate and g is the camera gain. The sky background is also Poisson noise and is due to the photons from the sky surrounding the star entering the pupil. The night sky is not void of light but instead can be described as a very dim, uniform surface. The sky background noise is calculated as,

$$N_{\text{sky}} = \sqrt{\frac{\text{sky}}{g}}, \tag{3.5}$$

with 'sky' being the counts in the aperture due to the background sky. n_{pix} is the number of pixels in a photometric aperture. N_{read} is the read noise per pixel which is approximately 7 ADU counts, although it is camera-dependent. This is another noise term that is unavoidable due to the imperfect nature of all CCDs. The final term is the scintillation term, using Equation 1.2 with the median value of $C_{\text{Y}} = 1.56$ for the Paranal Observatory. Since σ_{Y} is a fractional uncertainty I multiply by source count rate, f, to express it in ADU counts.

The visual inspection of the noise models against the RMS curve provides the opportunity to check for any major issues that may be present in the models used. Although the previous noise model was sufficient for the bright stars that it was applied to, I found during the course of the project that there was an error when it was applied to dim stars. Sky background counts were included in the scintillation term, i.e. $(\sigma_{\text{Y}} \times (f + \text{sky}))^2$, which then resulted in an overestimation of the scintillation when f and sky were of similar magnitudes. The physical reasoning for not including sky counts in the scintillation term is that the sky can be regarded as a uniform surface of light, emitting a given number of photons that are detected by the NGTS CCDs. Sky photons are scattered into and out of the telescope in equal measure by the scintillation effect, thus the net effect is zero scintillation due to the sky background.

Chapter 4

Results and Discussion

> And all this science, I don't understand
>
> —Elton John, Rocketman

This chapter outlines the results I find from analysing the RMS curves produced in Chapter 3.

4.1 Measurements of the empirical scintillation coefficient

I fit the total noise model (Equation 3.3) to the RMS curve for each star with the empirical scintillation coefficient, C_Y, as the only free parameter. I take the variance of the fit as our confidence level in the C_Y value. I plot a weighted histogram of all the C_Y values measured, using the reciprocal of the variance of the fit as the weightings. This is shown in Figure 4.1. I calculate a median of $C_Y = 1.54$ with lower and upper quartiles of 1.37 and 1.76, respectively. These values are in close agreement with the median C_Y value of 1.56 and quartiles of 1.27 and 1.90 for the Paranal Observatory from Osborn et al. (2015). This indicates that NGTS observations of bright stars can be used as a suitable method to measure scintillation above the Paranal Observatory.

The histogram shows a Gaussian-like distribution with a tail towards higher C_Y values. This is similar to the distribution shown in Figure 6 of Osborn et al. (2015). The authors used the SCIDAR instrument (Shepherd et al., 2014) to profile the atmosphere at La Palma and then estimated the scintillation noise for a 1 m telescope with a 1 s exposure time. Although the observatory and telescope specifications are different, I still retrieve the same distribution as expected.
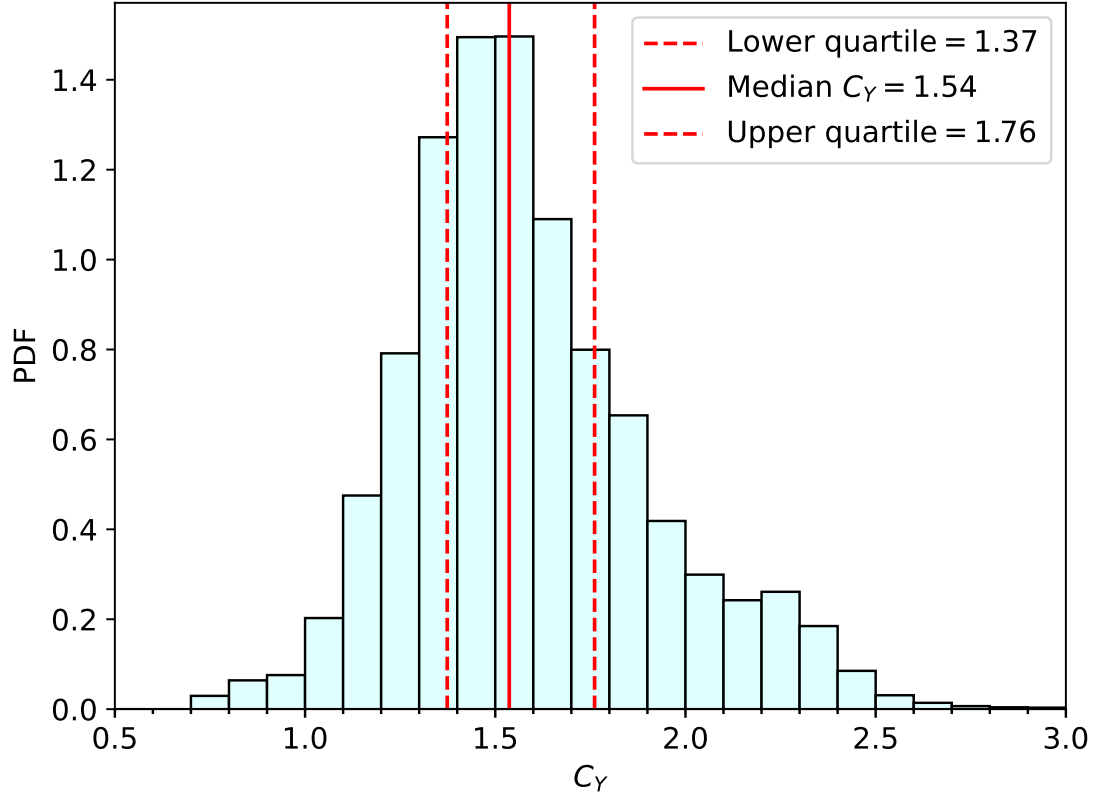
Figure 4.1: Normalized histogram of scintillation coefficients (C_Y) measured with the NGTS telescopes at the Paranal Observatory for all 21643 stars from 441 sub-actions across 122 nights. Values are weighted by $1/\sigma^2$, where σ^2 is the variance of the fit, and weights are normalized such that the area under the histogram equals 1. The solid red vertical line indicates the weighted median of the distribution ($C_Y = 1.54$) and the dashed lines indicate the lower and upper quartiles of 1.37 and 1.76.
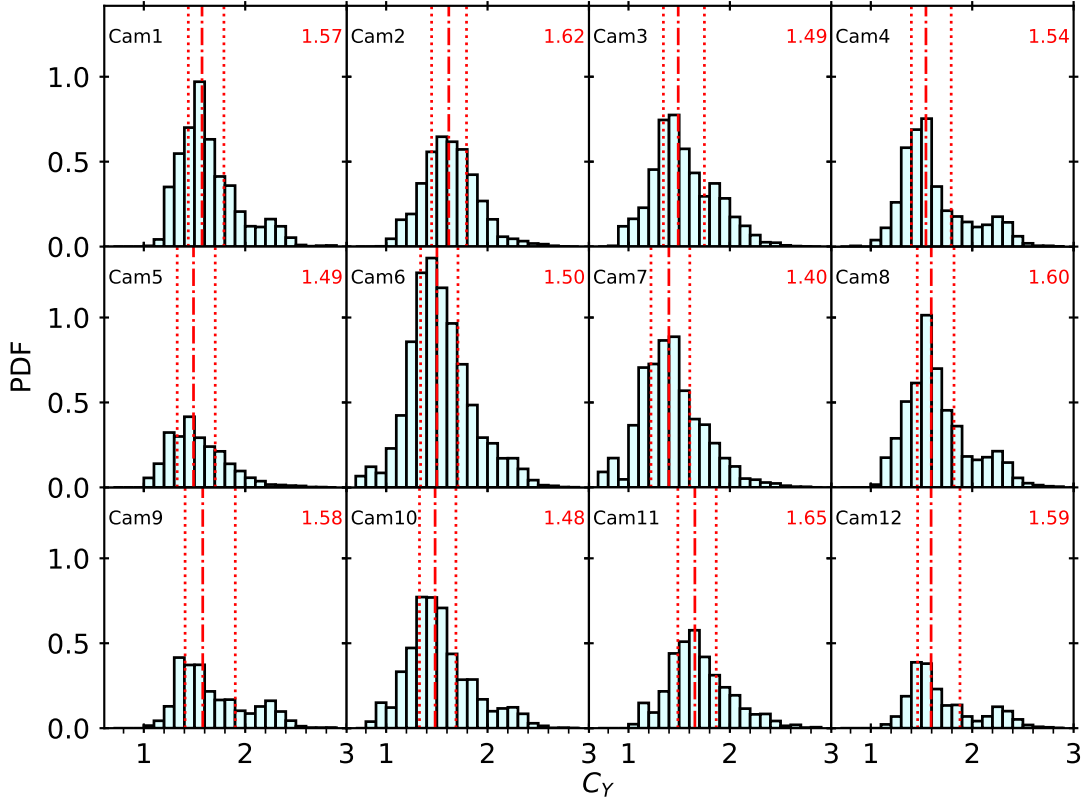
Figure 4.2: Normalized histograms displaying the C_Y values for all stars, split by camera. Each value used is weighted as in Section 4.1 and the weighted median is indicated by the red dash-dot lines, with the value displayed on each plot in red. The upper and lower quartiles for each camera are shown by vertical dotted lines. The histograms are normalized such that the relative size of histograms corresponds directly with the number of measurements, i.e. Cam6 took the most measurements for our sample.

4.2 Camera variability

The NGTS facility provides the opportunity to measure any camera-dependent systematic noise by using the measurements of scintillation from Section 4.1. Figure 4.2 shows histograms of the scintillation measurements made by each camera. This figure shows that generally the 12 NGTS cameras have a similar distribution of C_Y values and there is no significant difference in the measurements made by the individual instruments at the facility.

I note there is a minor peak at $C_Y = 2.3$ for some telescopes. This is caused by a relatively large amount of data being collected over a few nights with high scintillation.

33

These nights can be seen in Figure 4.3, in particular towards the end of our observation period. These measurements do not affect the overall conclusion that the cameras are operating as expected. An increased sample size would reduce the notability of these minor peaks.

I now combine C_Y values for all stars on each night for each MASS-DIMM target, but I treat each NGTS telescope measurement as an independent value. This gives one C_Y value per sub-action (Section 2.1). These C_Y values are computed as a weighted mean, using the weights as described in Section 4.1 and I calculate associated weighted standard deviations.

Figure 4.3 shows the inter-night variation between scintillation measurements made by the different NGTS cameras, also it shows the variation between nights of observation. This figure demonstrates that the difference between the values of C_Y measured by different telescopes is much less than the variation between different nights due to changes in the atmospheric turbulence. This indicates that we are making true measurements of the variation in scintillation.

4.3 Correlation of NGTS and MASS measurements

I tested for correlation between the scintillation strength measured by NGTS and the MASS-DIMM instruments' measurements. I use the mean C_Y values for each sub-action computed in Section 4.2, taking the median value on nights with multiple NGTS observations.

As discussed in Section 2.2, the MASS-DIMM changes target during the night and I have split the NGTS data to match this. I compute the mean MASS scintillation measurement for each of these sections of the night. The error on this mean MASS scintillation index is calculated as the standard error of the mean. I compare the correlation between the NGTS and MASS measurements by plotting the two datasets against each other, shown in Figure 4.4. The sky separation between the NGTS field center and MASS-DIMM target star, in degrees, is used to colour-code the plot.

As expected (see Section 1.2.1), we do not see strong correlation between the two measurements of scintillation since the MASS operates in the short-exposure regime while NGTS uses a long exposure time. I find a correlation coefficient of 0.22, indicating weak positive correlation. The lack of correlation could be due to wind speed variations on individual nights that have a greater effect on the long-exposure scintillation measurements made by NGTS. To test this would require calculating hourly NGTS scintillation measurements and comparing these values to higher temporal resolution ECMWF wind
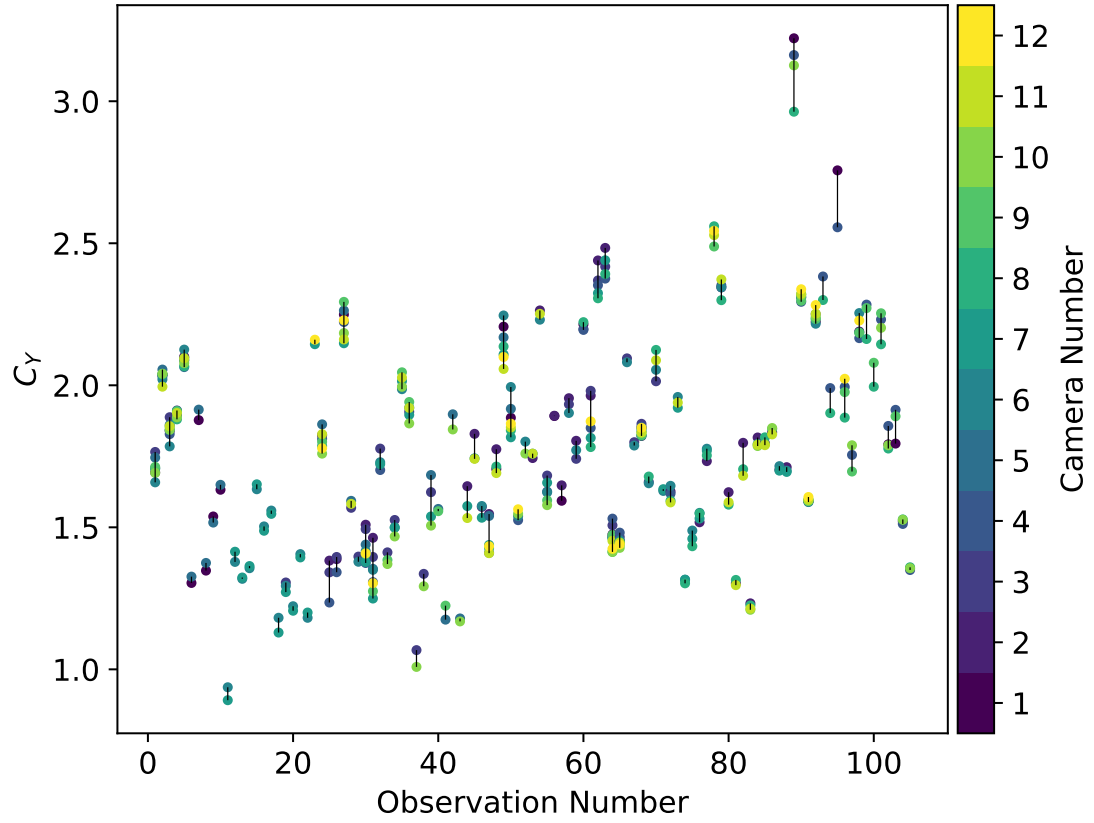
Figure 4.3: Scatter plot showing the value of C_Y for each sub-action, organised by night of observation. Only observation periods with multiple telescopes observing the same field are shown. Points are colour-coded by camera number using a discrete colourmap. Black vertical lines show the range of C_Y for each observation period.
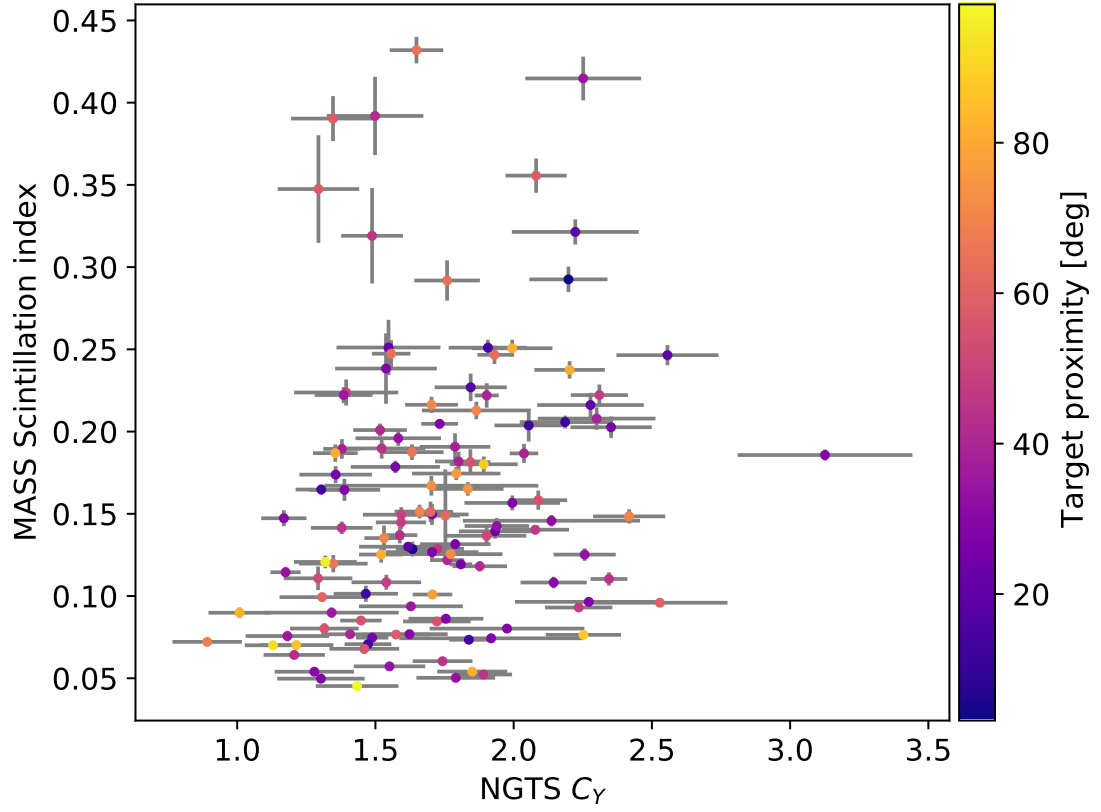
Figure 4.4: Scintillation coefficients (C_Y) measured by NGTS plotted against the scintillation indices measured by the MASS instrument. I plot all 122 nights for which NGTS observed bright stars, taking the median C_Y value for nights with multiple NGTS telescopes on the same target field. Colour-coded by separation between NGTS field center and MASS-DIMM target star.

speed data (Hersbach et al., 2018). Such an analysis could form the basis for future work.

We do not see a stronger correlation for targets that are closer in proximity. This suggests that the atmospheric conditions are consistent across the sky on a given night. This is supported by Kornilov et al. (2012) where they find a correlation between MASS scintillation measurements at nearby observing sites, for example Armazones and Paranal (approximately 20 km apart).

4.4   Seasonal variation in scintillation

The ERA5 dataset (Section 2.3, Hersbach et al. (2019)) provides information on the global wind velocity field, therefore I can use these data to test the relation between scintillation and high-altitude wind speeds. In Section 1.2, I explained how higher altitude turbulence has a greater effect on the scintillation measured by astronomical instruments. The ERA5 dataset has horizontal resolution of $0.25° \times 0.25°$ so we take the (U, V) wind components in the $1° \times 1°$ square centered on Paranal, $(\phi, \lambda) = (24.6°\text{S}, 70.4°\text{W})$. I calculate the wind speed at each point in the data grid as $\sqrt{U^2 + V^2}$ and compute the mean value of these wind speeds above the site for each month since January 2016.

4.4.1   Long-exposure scintillation

Figure 4.5 shows the annual variation in the NGTS C_Y measurements and the mean wind speed above Paranal, as computed from ECMWF data. The C_Y values for each sub-action as described in Section 4.2 are displayed as light grey points. For each month I then compute the mean value and standard deviation. ECMWF data are acquired as monthly-averaged data from January 2016 through until April 2021. The mean across the full 4-5 year period for each month is plotted, with corresponding standard deviation.

We can see that the NGTS measurements of C_Y, which acts as a proxy for the long-exposure scintillation index from Equation 1.3, show a minima in the months of June to August. The ECMWF wind speed measurements peak in these months. This indicates that long-exposure scintillation does indeed decrease in the southern hemisphere in the months of June and August, when the wind speeds in the upper atmosphere are higher. This is because the higher wind speed averages out the turbulence cells passing across the line-of-sight of the telescope during the long exposure time. This causes an averaging out of the variation of light intensity and therefore reduces scintillation. This is governed in Equation 1.3 as the $\frac{1}{V_\perp}$ term. I calculate a correlation coefficient of -0.65, indicating

37
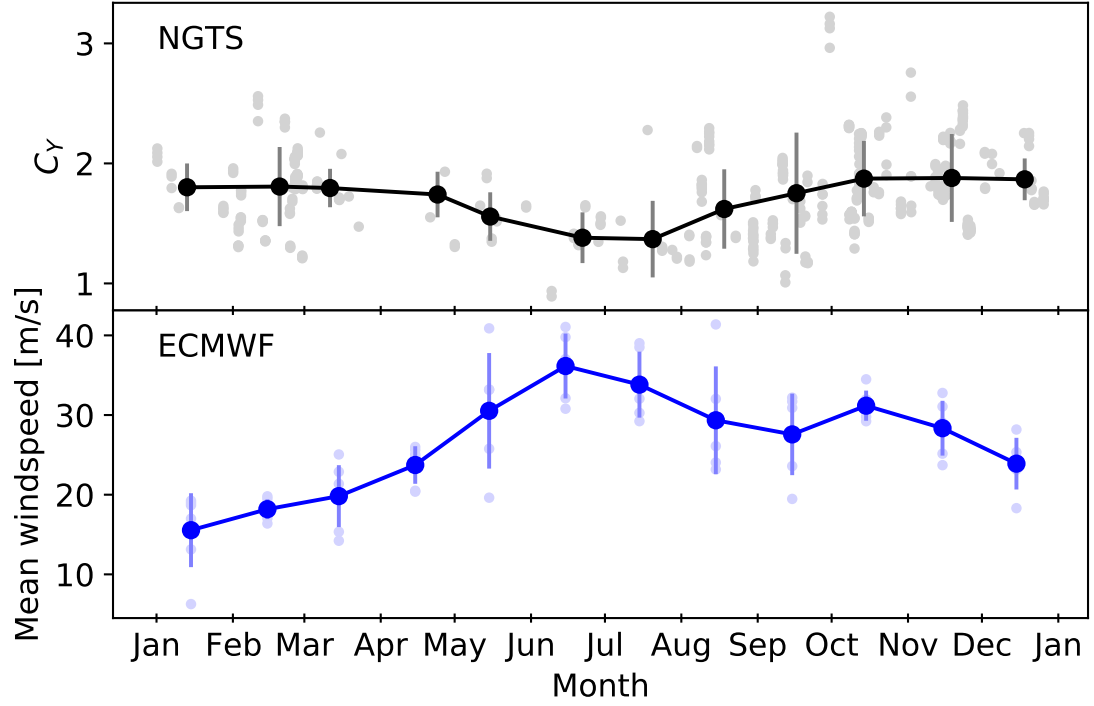
Figure 4.5: *Top panel*: NGTS measurements of C_Y folded onto a one-year period. Light grey points are the measurements for each sub-action and black circles show the mean for each month, with standard deviation shown as grey error bars. *Bottom panel*: ECMWF data for mean wind speed at $250\,\text{hPa}$ above Paranal. Faint blue points are the values for each month since 2016, blue circles are the mean values for each month across the full dataset with standard deviation shown as light blue error bars.
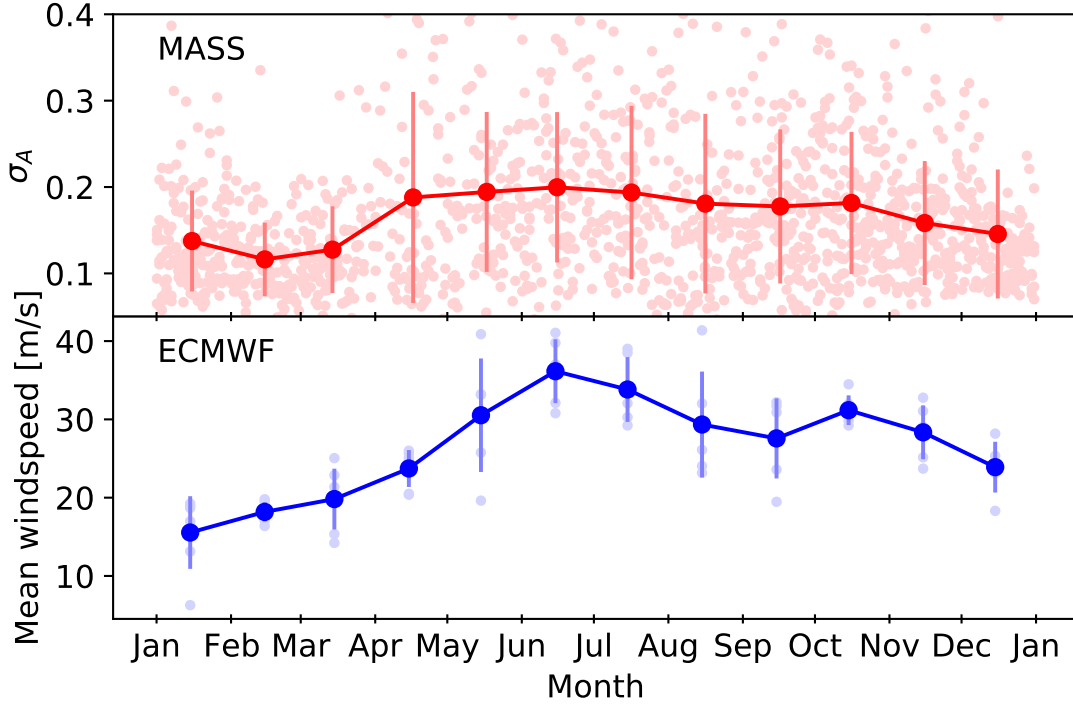
Figure 4.6: *Top panel*: MASS measurements of the scintillation index. Faint red points are the mean measurements of σ_A for each night (04/2016-03/2021), red circles show the monthly mean with standard deviation shown as light red error bars. *Bottom panel*: Same as bottom panel in Figure 4.5

moderately strong negative correlation between long-exposure scintillation and the mean wind speed.

Kornilov et al. (2012) determined that long-exposure scintillation is minimal from May to September. My conclusion is consistent with this. I also show the anti-correlation with high-altitude wind speed which is predicted by Kornilov et al. (2012).

4.4.2 Short-exposure scintillation

Figure 4.6 shows the annual changes in the scintillation index measured by the MASS from April 2016 to March 2021. I do note that the MASS data coverage is not uniform over these time periods due to operational interruptions. The ECMWF panel from Figure 4.5 is included to make comparison more simple.

It is evident from the top panel of Figure 4.6 that the short-exposure scintillation index increases in the months of April to July. Additionally, the standard devia-

tion, which indicates the variation in scintillation during the month, is much greater in these months. This suggests that scintillation conditions are much more unstable at the Paranal Observatory during these months. The peak in scintillation correlates with the peak in the high-altitude wind speeds measured by the ECMWF data. The higher wind speeds cause greater amounts of turbulence, therefore increasing $C_n^2(h)$. Meanwhile the short exposure time of the MASS measurements means that the averaging of the variation that occurs in the long-exposure regime is not a factor, consistent with the lack of a wind speed term in Equation 1.4. This increases the mean scintillation during these months. The instability in scintillation conditions is likely due to higher wind speeds being more likely but less sustainable during these months (Archer and Caldeira, 2008). I calculate a correlation coefficient of 0.86, indicating strong positive correlation between the MASS scintillation measurements and the mean wind speed.

It was found by Kornilov et al. (2012) that in the southern hemisphere the short-exposure scintillation is maximal in the period from July to September. I find a similar result however the peak is closer to being from May to July. I also show the increase in short-exposure scintillation does correlate with wind speed, as predicted by Kornilov et al. (2012).

Figures 4.5 and 4.6 also support their conclusions that the seasonal variability does not exceed the quartiles (or in our case standard deviations) which indicates there is a reasonable probability of both good and poor conditions for bright star photometry year-round (Kornilov et al., 2012).

Chapter 5

Conclusions

'I'm very into the universe, you know like how was
created, you know, like, what is it, you know? Solar
system is so humongous big, right? But if you see
like our solar system and our galaxy on the side,
you know, like, we're so small you can never see it.
Our galaxy is like huge, but if you see the big
picture our galaxy (is) like a small tiny-like dot in
the universe.'

—Ilya Bryzgalov, former hockey goaltender

In this thesis, I analyse the photometric precision of two years of NGTS bright
star observations from the Paranal Observatory. I find that the dominant source of
photometric noise for these stars is from atmospheric scintillation, and it is well described
by the modified Young's equation for low airmass (airmass < 1.5). Figure 4.1 shows a
Gaussian-like distribution for the empirical scintillation coefficient (C_Y), consistent with
SCIDAR-determined measurements presented in Figure 6 of Osborn et al. (2015). I find
the median value for the empirical scintillation coefficient at the Paranal Observatory
to be $C_\mathrm{Y} = 1.54$ with lower and upper quartiles of 1.37 and 1.76, respectively. This is
in good agreement with the value of $C_\mathrm{Y} = 1.56$ derived by Osborn et al. (2015) from
MASS measurements taken by Kornilov et al. (2012).

All 12 NGTS telescopes have a similar distribution of measured scintillation coef-
ficients, indicating that each individual telescope/camera reaches the scintillation limit
when observing bright stars (see Figure 4.2). Additionally, I find that the 12 NGTS
telescopes give consistent results for the measured scintillation when simultaneously ob-
serving the same field (see Figure 4.3). This indicates that the telescopes and cameras

are operating without any major source of camera-dependent systematic noise in this stellar magnitude regime.

As expected, we see no strong correlation between the NGTS and MASS measurements of scintillation (see Figure 4.4), owing to the fact that the instruments operate in different exposure time regimes (long-exposure and short-exposure regimes respectively).

This work provides observational evidence for the seasonal variation cycle in both the long-exposure and short-exposure scintillation regimes. In the long-exposure regime, I find that scintillation is minimal from June to August and I provide evidence that this seasonal variation correlates with the peak in high-altitude wind speed above the Paranal Observatory (see Figure 4.5). This is likely due to the turbulence cells being averaged out as they pass across the telescopes line-of-sight during the 10 s exposure time of the NGTS cameras. In the short-exposure regime, I find that scintillation is maximal from April to July. This peak matches with the peak in high-altitude wind speed which increases the turbulence strength, while the short-exposure time of the MASS instrument means there is no averaging out of the turbulence cells (see Figure 4.6).

The results of scintillation studies can be applied to the field of satellite laser communications, which plan to use optical bandwidth lasers for transmitting data to the ground. Such communications are subject to the same atmospheric scintillation that I probe in this study.

In this thesis, I have demonstrated that NGTS bright star observations reach the scintillation limit and can be used to measure changes in scintillation above Paranal. This is an example of the wealth of site characterisation data that lies hidden in archival datasets. This work can be extended to any observatory with telescopes that reach the scintillation limit, thus providing an alternative method for characterising atmospheric conditions without any need for additional instrumentation or dedicated telescope time.

5.1 Future work

5.1.1 NGTS-MASS hourly wind speed analysis

I hypothesised in Section 4.3 that the lack of correlation in Figure 4.4 could be due to wind speed variations on individual nights that have a greater effect on the long-exposure scintillation measurements made by NGTS. The ECMWF hosts a dataset titled 'ERA5 hourly data on pressure levels from 1979 to present' (Hersbach et al., 2018). This dataset provides us with the time resolution required to test this hypothesis. The primary difference between Equation 1.3 and Equation 1.4 is that the former has a wind speed

term. This suggests that the ratio of hourly NGTS and MASS measurements would correlate with the wind speed above Paranal at the 250 hPa level. An analysis of this would require hourly NGTS scintillation measurements and the processing of the large dataset of wind speed data. This could form the basis for a future study. If it is found that changes in NGTS scintillation measurements correlate strongly with wind speed variations on individual nights then we could potentially predict the expected scintillation conditions at Paranal prior to observing by using weather forecasts of high-altitude wind speeds.

5.1.2 NGTS Scintillation monitoring

Routinely taking measurements of C_Y for each action can be implemented as an additional step in the bright stars pipeline and will be useful for informing the NGTS consortium of the quality of observations at the facility. This consistent analysis will allow us to build up the number of measurements of C_Y that we have across a longer time period. This will result in the possibility of even more robust testing of the one-year cycle in the C_Y values found in Section 4.4.1. Furthermore, comparisons with the ERA5 dataset will further strengthen the evidence for the link between monthly wind speed averages and long-exposure scintillation.

It is also plausible that with a greater number of observations spanning all months of the year, we may well find stronger correlation between NGTS (long-exposure) and MASS (short-exposure) scintillation measurements in the intermediate months between the opposing peaks and troughs in these two scintillation regimes. Considering the top panels of Figures 4.5 and 4.6, the dip in NGTS C_Y values is around July and the peak lies close to December-January. Meanwhile, the MASS scintillation indices peak around July while the dip is in February. Therefore it is plausible that there exists months in between these extrema when the NGTS and MASS measurements 'cross' and we could find stronger correlation in these months. Preliminary tests of this hypothesis found that the sample size for some months was too small but more observations would provide the opportunity to test this further. If a strong correlation is found then we can use MASS scintillation measurements as a strong indicator of scintillation conditions during these months.

In addition, more observations at higher airmass (airmass > 1.5) would allow more robust testing of the airmass-dependency in the modified Young's equation (Eq. 1.2). This would require a dedicated observing campaign as NGTS normally avoids higher airmass observations when attempting to acquire high-precision time-series pho-

43

Observatory	Latitude	Longitude	Altitude (m)	C_Y
Paranal, Chile	24.6°S	70.46°W	2440	$1.56^{+0.34}_{-0.29}$
La Palma, Spain	28.76°N	17.96°W	2396	$1.30^{+0.32}_{-0.28}$
Mauna Kea, HI, USA	19.96°N	155.56°W	4205	$1.63^{+0.39}_{-0.29}$

Table 5.1: Coordinates of major astronomical observatories

tometry for astrophysical research.

In addition to using single telescope observations and multi-telescope observations of the same field of stars, it may be interesting to schedule bright star observations of multiple fields simultaneously and comparing the short-term (of order seconds to minutes) variation in scintillation. This has the potential to track turbulence cells passing across the site with a time lag existing for the scintillation measured by different cameras. Alternatively, this would support the conclusion in Section 4.4.2 that the atmospheric conditions are consistent across the sky on a given night.

5.1.3 Additional site monitoring

The work on seasonal scintillation variation can be extended to monitoring of other observing sites. Along with Paranal Observatory in Chile, the Mauna Kea Observatories in Hawaiʻi and the Roque de los Muchachos Observatory on La Palma in the Canary Islands are the primary observing sites of the astronomical community. The coordinates and altitudes of each of these observatories are displayed in Table 5.1. In addition, I also give the median C_Y values, with upper and lower quartiles, as derived by Osborn et al. (2015).

All three observatories are at similar latitudes (with Paranal in the southern hemisphere) therefore they will be effected to some extent by the position of the sub-tropical jet streams in their hemisphere. The jet streams are strongest in the respective winters of each hemisphere (recall the southern hemisphere winter is June to August) as the temperature gradient between high and mid-level latitudes, which drives the jet streams, is greater (Archer and Caldeira, 2008). This is evident in Figure 5.1. This figure shows the mean wind speeds each month since 2016 in the $1° \times 1°$ square centered on each observatory, using ECMWF data (see Sections 2.3 and 4.4).

In Figure 5.1, we see that since Paranal Observatory (red, dash-dot line) is in the southern hemisphere, the peak wind speeds are offset by six months compared to the two northern hemisphere sites. Furthermore, La Palma experiences greater peaks in the mean wind speed above the site, likely due to its higher latitude location being more
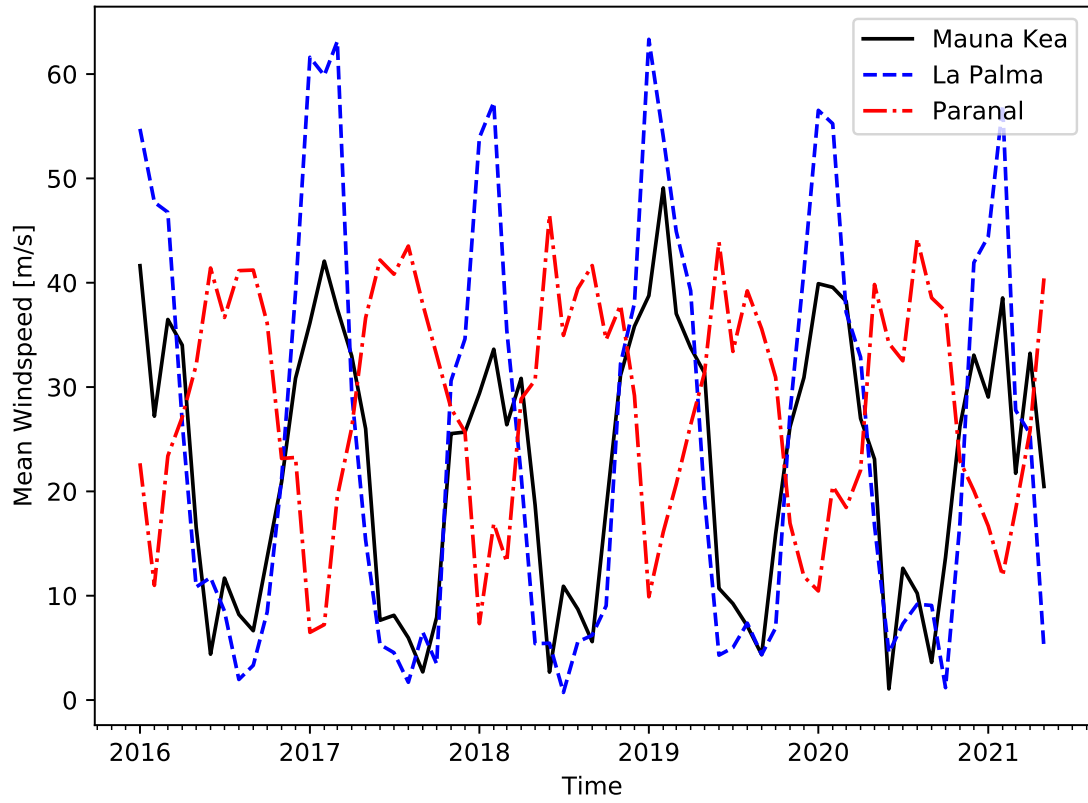
Figure 5.1: Mean wind speeds at 250 hPa for different observing sites using ECMWF data. Mauna Kea is a black solid line; La Palma is a blue dotted line; Paranal is a red dash-dot line. Major ticks of each year denote the start of the year.

directly beneath the core of the northern subtropical jet stream in the winter months. In the time span displayed, Mauna Kea saw a greater variety in the size of the winter peaks with a 'lingering jet stream' in the winter of 2019 that was stronger than usual and did cause unusual weather events for the islands[a].

The effects this will have on scintillation can be extrapolated from the findings of Section 4.4.1. The higher wind speeds cause a decrease in long-exposure scintillation. Therefore we can expect that La Palma has excellent long-exposure scintillation conditions in the winter months of December to February. Indeed the lower site median for scintillation of $C_Y = 1.30$ indicates that scintillation is generally lower at La Palma. Mauna Kea was found to exhibit annually-stable scintillation conditions in Kornilov et al. (2012) and we can speculate that this likely will be the case due to the smaller amplitude of the peaks in wind speed. The abnormally high peak in 2019 is likely to be an anomaly although a longer baseline of data would be required to make such a conclusion. The higher altitude of Mauna Kea is also a minor factor in the altitude and pressure of the jet stream but also the resulting scintillation effect. The spatial extent of the scintillation speckles is directly linked to propagation distance so the higher altitude will result in a slightly smaller propagation distance, however this is beyond the scope of this thesis. The proposed stability of the scintillation at Mauna Kea is marginally contradictory to the larger interquartile range for C_Y found in Osborn et al. (2015), however it is not significantly larger and more observations would be required to make better conclusions. The higher troughs of the mean wind speeds for Paranal (i.e. higher wind speeds than the northern sites when comparing respective summers) also suggests that Paranal Observatory is a stable site with good scintillation conditions year-around as the difference between winter and summer wind speeds is smaller.

In order to test these theories, we would require a catalogue of bright star observations by small-aperture telescopes, similar to NGTS, at both of these sites. In addition to investigating long-exposure variation, access of MASS-DIMM data at other observatories would provide a test of the short-exposure variation (Section 4.4.2). Most major observatories operate a MASS-DIMM system so this data will hopefully be accessible.

---

[a]The Guardian article: https://www.theguardian.com/us-news/2019/feb/11/snow-hawaii-maui-seattle-winter-storm

5.1.4 Final outlook

Scintillation is an unavoidable source of photometric noise for ground-based telescopes, such as NGTS. However, the practicalities and smaller financial cost of ground-based facilities, when compared with their space-based counterparts, means that we must continue to improve our understanding of the scintillation effect. Further research into the scintillation effect will allow us to understand our data more fully, increasing the accuracy with which we can measure planetary radii; determine transit timing variations; and better plan our observation strategies. In addition to these results, we will also gain a better understanding of the changes in the Earth's atmosphere above observatories. This information can then potentially be used in future advancements in optical laser communications and even modelling of weather systems to improve forecasting.

Bibliography

Andrews, L.C. and Phillips, R.L. Impact of scintillation on laser communication systems: recent advances in modeling. In Voelz, D.G. and Ricklin, J.C., editors, *Free-Space Laser Communication and Laser Imaging*, volume 4489 of *Society of Photo-Optical Instrumentation Engineers (SPIE) Conference Series*, pages 23–34, January 2002. doi: 10.1117/12.453235.

Archer, C.L. and Caldeira, K. Historical trends in the jet streams. *Geophysical Research Letters*, 35(8), 2008. doi: https://doi.org/10.1029/2008GL033614. URL `https://agupubs.onlinelibrary.wiley.com/doi/abs/10.1029/2008GL033614`.

Aristotle. De Caelo. In J.L.Stocks, editor, *Book 2*. OUP, 350 BC. URL `https://archive.org/stream/decaeloleofric00arisuoft/decaeloleofric00arisuoft_djvu.txt`. chap. 8, para. 290a, 18.

Armstrong, D.J. et al. A remnant planetary core in the hot-Neptune desert. *Nature*, 583(7814):39–42, July 2020. doi: 10.1038/s41586-020-2421-7.

Astropy Collaboration et al. Astropy: A community Python package for astronomy. *A&A*, 558:A33, October 2013. doi: 10.1051/0004-6361/201322068.

Astropy Collaboration et al. The Astropy Project: Building an Open-science Project and Status of the v2.0 Core Package. *AJ*, 156(3):123, September 2018. doi: 10.3847/1538-3881/aabc4f.

Babcock, H.W. The Possibility of Compensating Astronomical Seeing. *PASP*, 65(386): 229, October 1953. doi: 10.1086/126606.

Bayliss, D. et al. NGTS-1b: a hot Jupiter transiting an M-dwarf. *MNRAS*, 475(4): 4467–4475, April 2018. doi: 10.1093/mnras/stx2778.

Beattie, J. and Kriel, N. Is The Starry Night Turbulent? *arXiv e-prints*, art. arXiv:1902.03381, February 2019.

Borucki, W.J. et al. Kepler Planet-Detection Mission: Introduction and First Results. *Science*, 327(5968):977, February 2010. doi: 10.1126/science.1185402.

Brahm, R. et al. TOI-481 b and TOI-892 b: Two Long-period Hot Jupiters from the Transiting Exoplanet Survey Satellite. *AJ*, 160(5):235, November 2020. doi: 10.3847/1538-3881/abba3b.

Brown, T.M. and Gilliland, R.L. Asteroseismology. *ARA&A*, 32:37–82, January 1994. doi: 10.1146/annurev.aa.32.090194.000345.

Bruno, G. *On the Infinite, the Universe, & the Worlds / De I'Infinito, Universe, E Mondi.* Collected Works of Giordano Bruno. Createspace Independent Pub, 1584. ISBN 9781500826314. URL `https://books.google.co.uk/books?id=AhWzoQEACAAJ`. Translated by Gosnell, S. Published 2014.

Bryant, E.M. et al. Simultaneous TESS and NGTS transit observations of WASP-166 b. *MNRAS*, 494(4):5872–5881, April 2020. doi: 10.1093/mnras/staa1075.

Bryant, E.M. et al. A transit timing variation observed for the long-period extremely low-density exoplanet HIP 41378 f. *MNRAS*, 504(1):L45–L50, June 2021. doi: 10.1093/mnrasl/slab037.

Cassan, A. et al. One or more bound planets per Milky Way star from microlensing observations. *Nature*, 481(7380):167–169, January 2012. doi: 10.1038/nature10684.

Chiozzi, G. et al. The ESO astronomical site monitor upgrade. In Chiozzi, G. and Guzman, J.C., editors, *Software and Cyberinfrastructure for Astronomy IV*, volume 9913 of *Society of Photo-Optical Instrumentation Engineers (SPIE) Conference Series*, page 991314, August 2016. doi: 10.1117/12.2232302.

Dhillon, V.S. et al. HiPERCAM: a high-speed quintuple-beam CCD camera for the study of rapid variability in the universe. In Evans, C.J., Simard, L. and Takami, H., editors, *Ground-based and Airborne Instrumentation for Astronomy VI*, volume 9908 of *Society of Photo-Optical Instrumentation Engineers (SPIE) Conference Series*, page 99080Y, August 2016. doi: 10.1117/12.2229055.

Dravins, D. et al. Atmospheric Intensity Scintillation of Stars, I. Statistical Distributions and Temporal Properties. *PASP*, 109:173–207, February 1997. doi: 10.1086/133872.

Ellison, M.W. Why do Stars Twinkle? *Irish Astronomical Journal*, 2:5, March 1952.

Föhring, D. et al. Atmospheric scintillation noise in ground-based exoplanet photometry. *MNRAS*, 489(4):5098–5108, November 2019. doi: 10.1093/mnras/stz2444.

Gaia Collaboration et al. The Gaia mission. *A&A*, 595:A1, November 2016. doi: 10.1051/0004-6361/201629272.

Haguenauer, P., Guesalaga, A. and Butterley, T. Comparison of atmosphere profilers at Paranal and atmosphere parameters statistics: AOF-profiler, STEREO-SCIDAR, MASS-DIMM, LGS-WFS. In *Society of Photo-Optical Instrumentation Engineers (SPIE) Conference Series*, volume 11448 of *Society of Photo-Optical Instrumentation Engineers (SPIE) Conference Series*, page 114481K, December 2020. doi: 10.1117/12.2562267.

Heasley, J.N. et al. The Prospects for Asteroseismology from Ground-based Sites. *PASP*, 108:385, May 1996. doi: 10.1086/133737.

Hersbach, H. et al. ERA5 hourly data on pressure levels from 1979 to present. , 2018. Copernicus Climate Change Service (C3S) Climate Data Store (CDS). doi: 10.24381/cds.bd0915c6.

Hersbach, H. et al. ERA5 monthly averaged data on pressure levels from 1979 to present., 2019. Copernicus Climate Change Service (C3S) Climate Data Store (CDS). Accessed on 06-May-2021. doi: 10.24381/cds.6860a573.

Jiang, L. et al. Analysis of scintillation effects along a7 km urban space laser communication path. *Appl. Opt.*, 59(27):8418, September 2020. doi: 10.1364/AO.397309.

Kenyon, S.L. et al. Atmospheric Scintillation at Dome C, Antarctica: Implications for Photometryand Astrometry. *PASP*, 118(844):924–932, June 2006. doi: 10.1086/505409.

Kolmogorov, A. The Local Structure of Turbulence in Incompressible Viscous Fluid for Very Large Reynolds' Numbers. *Akademiia Nauk SSSR Doklady*, 30:301–305, January 1941.

Kornilov, V. et al. Combined MASS-DIMM instruments for atmospheric turbulence studies. *MNRAS*, 382(343):1268–1278, December 2007. doi: 10.1111/j.1365-2966.2007.12467.x.

Kornilov, V. et al. Comparison of the scintillation noise above different observatories measured with MASS instruments. *A&A*, 546:A41, October 2012. doi: 10.1051/0004-6361/201219954.

Lerner, R. and Trigg, G. *Encyclopedia of Physics*. VCH, 1991. ISBN 9783527269549. URL `https://books.google.co.uk/books?id=bNYPAQAAMAAJ`.

Marois, C. et al. Direct Imaging of Multiple Planets Orbiting the Star HR 8799. *Science*, 322(5906):1348, November 2008. doi: 10.1126/science.1166585.

Marshak, A. and Davis, A. *3D Radiative Transfer in Cloudy Atmospheres*. Physics of Earth and Space Environments. Springer Berlin Heidelberg, 2006. ISBN 9783540285199. URL `https://books.google.co.uk/books?id=NR8yY6M6I2QC`.

May, B.H. *A survey of radial velocities in the zodiacal dust cloud*. PhD thesis, Imperial College London, October 2007.

Mayor, M. and Queloz, D. A Jupiter-mass companion to a solar-type star. *Nature*, 378 (6555):355–359, November 1995. doi: 10.1038/378355a0.

McCormac, J. et al. The Next Generation Transit Survey—Prototyping Phase. *PASP*, 129(972):025002, February 2017. doi: 10.1088/1538-3873/129/972/025002.

O'Brien, S.M. et al. Scintillation-limited photometry with the 20-cm NGTS telescopes at Paranal Observatory. *MNRAS*, 509(4):6111–6118, February 2022. doi: 10.1093/mnras/stab3399.

Osborn, A. et al. TOI-431/HIP 26013: a super-Earth and a sub-Neptune transiting a bright, early K dwarf, with a third RV planet. *MNRAS*, 507(2):2782–2803, October 2021. doi: 10.1093/mnras/stab2313.

Osborn, J. Scintillation correction for astronomical photometry on large and extremely large telescopes with tomographic atmospheric reconstruction. *MNRAS*, 446(2):1305–1311, January 2015. doi: 10.1093/mnras/stu2175.

Osborn, J. et al. Atmospheric scintillation in astronomical photometry. *MNRAS*, 452 (2):1707–1716, September 2015. doi: 10.1093/mnras/stv1400.

Osborn, J. *Profiling the turbulent atmosphere and novel correction techniques for imaging and photometry in astronomy*. PhD thesis, Durham University, Centre for Advanced Instrumentation, August 2010.

Osborn, J. et al. Conjugate-plane photometry: reducing scintillation in ground-based photometry. *MNRAS*, 411(2):1223–1230, February 2011. doi: 10.1111/j.1365-2966.2010.17759.x.

Perryman, M. et al. Astrometric Exoplanet Detection with Gaia. *ApJ*, 797(1):14, December 2014. doi: 10.1088/0004-637X/797/1/14.

Pollacco, D.L. et al. The WASP Project and the SuperWASP Cameras. *PASP*, 118 (848):1407–1418, October 2006. doi: 10.1086/508556.

Ricker, G.R. et al. Transiting Exoplanet Survey Satellite (TESS). *Journal of Astronomical Telescopes, Instruments, and Systems*, 1:014003, January 2015. doi: 10.1117/1.JATIS.1.1.014003.

Roddier, F. The effects of atmospheric turbulence in optical astronomy. *Progess in Optics*, 19:281–376, January 1981. doi: 10.1016/S0079-6638(08)70204-X.

Sachs, A. Babylonian Observational Astronomy. *Philosophical Transactions of the Royal Society of London Series A*, 276(1257):43–50, May 1974. doi: 10.1098/rsta.1974.0008.

Shepherd, H.W. et al. Stereo-SCIDAR: optical turbulence profiling with high sensitivity using a modified SCIDAR instrument. *MNRAS*, 437(4):3568–3577, February 2014. doi: 10.1093/mnras/stt2150.

U.S. COESA. U.S. Standard Atmosphere, 1976. Unknown, October 1976.

van Gogh, V. The Starry Night, 1889. Museum of Modern Art, New York City. Accessed: 26-05-2021 from https://commons.wikimedia.org.

Viotto, V. et al. MCAO: Wavefront sensing only as a tool for high precision photometry? In Ellerbroek, B.L., Marchetti, E. and Véran, J.P., editors, *Adaptive Optics Systems III*, volume 8447 of *Society of Photo-Optical Instrumentation Engineers (SPIE) Conference Series*, page 84476X, July 2012. doi: 10.1117/12.926370.

Wheatley, P.J. et al. The Next Generation Transit Survey (NGTS). *MNRAS*, 475(4): 4476–4493, April 2018. doi: 10.1093/mnras/stx2836.

White, R.H., Battisti, D.S. and Roe, G.H. Mongolian Mountains Matter Most: Impacts of the Latitude and Height of Asian Orography on Pacific Wintertime Atmospheric Circulation. *Journal of Climate*, 30(11):4065–4082, June 2017. doi: 10.1175/JCLI-D-16-0401.1.

Whitney, C.A. The Skies of Vincent van Gogh. *Art History*, 9(3):351–362, 1986. doi: https://doi.org/10.1111/j.1467-8365.1986.tb00206.x. URL `https://onlinelibrary.wiley.com/doi/abs/10.1111/j.1467-8365.1986.tb00206.x`.

Winn, J.N. *Exoplanet Transits and Occultations*, pages 55–77. University of Arizona Press, 2010.

Wolszczan, A. and Frail, D.A. A planetary system around the millisecond pulsar PSR1257 + 12. *Nature*, 355(6356):145–147, January 1992. doi: 10.1038/355145a0.

Young, A.T. Photometric error analysis. VI. Confirmation of Reiger's theory of scintillation. *AJ*, 72:747, August 1967. doi: 10.1086/110303.